Photocatalytic activation of peroxymonosulfate (PMS) by novel mesoporous Ag/ZnO@$NiFe_2O_4$ nanorods, inducing radical-mediated Acetaminophen degradation under UVA irradiation

Mona Kohantorabi[1], Gholamreza Moussavi[1*], Samira Mohammadi[1], Paula Oulego[2], Stefanos Giannakis[3]

1) Department of Environmental Health Engineering, Faculty of Medical Sciences, Tarbiat Modares University, Tehran, Iran.

2) Department of Chemical and Environmental Engineering, University of Oviedo, C/ Julián Clavería s/n., Oviedo, E-33071, Spain.

3) Universidad Politécnica de Madrid, E.T.S. Ingenieros de Caminos, Canales y Puertos, Departamento de Ingeniería Civil: Hidráulica, Energía y Medio Ambiente, Unidad docente Ingeniería Sanitaria, c/ Profesor Aranguren, s/n, ES-28040 Madrid, Spain.

***Corresponding author**: Prof. Dr. Gholamreza Moussavi, **E-mail**: moussavi@modares.ac.ir*

Published in "Chemosphere", Elsevier:

https://www.sciencedirect.com/science/article/pii/S0045653521007402

Permanent address (DOI):

https://doi.org/10.1016/j.chemosphere.2021.130271

Abstract

A new mesoporous Ag/ZnO@$NiFe_2O_4$ nanorod was prepared by a facile, low-cost, and environmentally friendly strategy from a bimetallic Fe_2Ni-MIL-88 metal organic framework (MOF), as an effective catalyst and peroxymonosulfate (PMS) photo-activator. The structural, morphological, optical, and magnetic properties, as well as the material composition were investigated by XRD, FE-SEM, EDX, HR-TEM, XPS, DRS, PL, EIS, VSM, N_2 adsorption-desorption and ICP-AES analysis. 1.0% w/w loading of Ag nanoparticles on $ZnO_{0.04}$@$NiFe_2O_4$ led to the best catalytic activity for PMS activation under UVA in acetaminophen (ACT) degradation. The maximum degradation efficiency for ACT was 100% within 15 min (at pH = 7.0), with a first-order rate constant of 0.368 min^{-1}. The calculated quantum yield (1.3×10^{-3} molecule/photon) of the optimum catalyst was 2.05, and 5.63 times higher than its simple constituents, $ZnO_{0.04}$@$NiFe_2O_4$ and $NiFe_2O_4$, respectively. Among the various inorganic ions, Cl^- and HCO_3^- showed significant inhibition effect in 1.0%w/w Ag/$ZnO_{0.04}$@$NiFe_2O_4$/PMS/UVA system, due to radical quenching effects. Based on scavenger experiments, $HO^\bullet$ and $SO_4^{\bullet-}$ were the dominant reactive species in photocatalytic process coupled with PMS. Due to presence of the Fe^{3+}/Fe^{2+}, and Ni^{2+}/Ni^{3+} reaction cycles in the as-made catalyst, the reaction rate of PMS activation was greatly enhanced. Moreover, the formation of a hetero-junction structure with $NiFe_2O_4$ and ZnO promoted the charge separation of the photo-generated electron/hole pairs. Finally, the major intermediates produced during the reaction were detected by LC-MS analysis, and a plausible mechanism for the photocatalytic degradation of ACT was proposed and discussed in detail.

Keywords: *Advanced oxidation process, Peroxymonosulfate activation, Photocatalysis, Metal Organic Frameworks, Emerging contaminants.*

Abbreviations

SR-AOP - sulfate radical based advanced oxidation processes; PMS - peroxymonosulfate; PDS - peroxydisulfate; PCO - photocatalytic oxidation; ROS - reactive oxygen species; MOFs - Metal organic frameworks; NPs - nanoparticles; ACT - acetaminophen; TOC - total organic carbon; SD - Standard deviation; PFO - pseudo-first order; CB - conduction band; VB - valence band

Highlights

- A novel ZnO@$NiFe_2O_4$ nanorod was synthesized from Fe_2Ni-MIL-88 by a facile chemical route.
- The presence of Ag NPs increased ACT degradation in the Ag/ZnO@$NiFe_2O_4$/PMS/UVA process.
- Ag/ZnO@$NiFe_2O_4$/PMS/UVA process is an efficient, radical based system (dominant $SO_4^{\bullet-}$ and $HO^{\bullet}$).
- Highly synergic ACT oxidation rate was obtained in the Ag/ZnO@$NiFe_2O_4$/PMS/UVA process.
- The catalyst was stable over repeated UVA/PMS-assisted photocatalytic ACT degradation.

Graphical Abstract

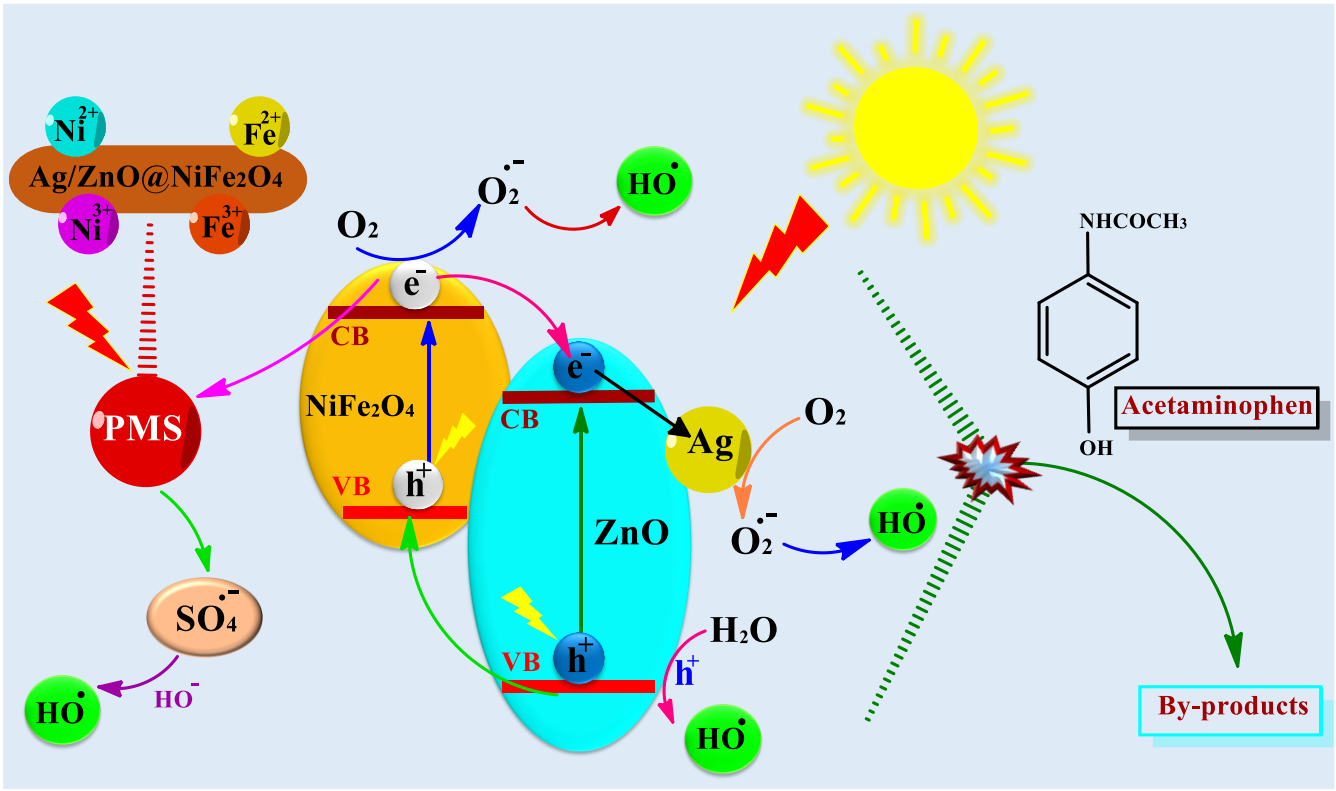

1. Introduction

Over the last years recent years, sulfate radicals based advanced oxidation processes (SR-AOP) include sulfate ($SO_4^{\bullet-}$), and hydroxyl ($HO^{\bullet}$) radicals was developed for environmental protection applications (Zhang et al., 2016; Giannakis et al. 2021a). Among the different oxidants that can produce $SO_4^{\bullet-}$, we encounter peroxymonosulfate (PMS) and peroxydisulfate (PDS). PMS is a relatively strong oxidant by itself and widely applied in AOPs, due to its environmentally compatible character (Guan et al., 2018). Compared with PDS, activation of PMS is easier, thanks to its asymmetrical structure, and can simultaneously produce $SO_4^{\bullet-}$ and $HO^{\bullet}$ (Hu and Long, 2016). Its use in SR-AOPs presents advantages such as long half lifetime (30-40 µs for $SO_4^{\bullet-}$ *vs*. 20 ns for $HO^{\bullet}$), high stability, high oxidation potential for $SO_4^{\bullet-}$ and $HO^{\bullet}$ (2.5–3.1 V and 1.8–2.7 V *vs*. NHE, respectively) and the possibility to be effective at a wide range of pH values (Kohantorabi et al., 2021a; Wang et al., 2019). This oxidant can be activated by various methods such as heat, UV irradiation, ultrasound, metal ions (Fe^{2+}, Co^{2+}, Mn^{2+}, Cu^{2+}, Ce^{3+}, Ni^{2+}, etc.), photo-catalysis and bases (Wang et al., 2016; Giannakis et al. 2021b).

Many homogenous and heterogeneous catalytic systems have been studied for PMS and PDS activation (Rodriguez-Chueca et al., 2019; Li et al., 2019). Due to some intrinsic disadvantages, including the difficulty in catalyst recovery and metal ions leaching into the reaction media causing secondary water pollution, the application of homogenous catalysts is relatively limited (Kohantorabi and Gholami, 2017). For this reason, heterogeneous catalytic systems, such as the use of nanoparticles (NPs) and metal oxides have emerged as potential candidates for replacing the homogeneous processes (Xu et al., 2020a). Among the various transition metals which can activate PMS, Co^{2+} ions are the most effective, but have toxic effect in water, hence the application of Co-based catalysts is not widely adopted (Khan et al., 2017). Therefore, it is important to devise proper ways to use more environmentally friendly, low-cost, albeit efficient metallic catalysts for these applications. Recently, magnetic-based catalysts, such as MFe_2O_4 (M = Co, Fe, Zn, Mn, and Cu) (Huang et al., 2019, Liu et al., 2015, Zhu et al., 2016) and metal oxides (*e.g.*, MnO_2, CuO, Fe_2O_3, CeO_2, Co_3O_4) were used for the catalytic activation of PMS in wastewater treatment, presenting an alternative to Co use (Khan et al., 2017, Zhu et al., 2016; Ding et al., 2020; Shen et al., 2020).

Photocatalytic oxidation (PCO) is an interesting intensification approach in AOPs, owing to the generation reactive oxygen species (ROS). In fact, photocatalysts not only can generate the electron/hole (e^-/h^+) pairs under light irradiation, but also enhance the efficiency of reactions by producing ROS, such as superoxide ($O_2^{\bullet -}$), and $HO^{\bullet}$ (Reza et al., 2020). Metal organic frameworks (MOFs) which are formed by metal ions and organic linkers/or clusters, have been widely used in photocatalysis. MOFs are a category of porous materials with excellent properties, such as controllable porosity, high surface area and active sites (Kohantorabi and Gholami, 2017). In recent years, they have demonstrated their capacity as an ideal template for the direct preparation of metal oxides. For example, various metal oxides including CeO_2, Fe_2O_3, Cr_2O_4, and $NiFe_2O_4$ were synthesized by using Ce (1,3,5-BTC) $(H_2O)_6$ MOF (Kohantorabi and Gholami, 2017), Cr-Fe-BTC MOF (Salari, 2019), and Fe_2Ni-MIL-88 (Li et al., 2020) as templates, respectively. $NiFe_2O_4$ as a semiconductor was studied and applied in photocatalytic reactions as well (Sudhaik et al., 2018). However, the fast recombination of photo-generated e^-/h^+ pairs in the pure $NiFe_2O_4$ nanostructure hampers its photocatalytic activity. Therefore, different strategies have been studied to alleviate the inherent issues of the photocatalytic performance of $NiFe_2O_4$ (Sakhare et al., 2020).

The combination of two or three semiconductors can improve the activity and efficiency of nanostructures and thus impulse their use in photocatalytic applications. An efficient photocatalyst has vital properties, such as suitable electronic structure, high quantum efficiency, high extinction coefficient and environmentally friendly behavior (Khavar et al., 2019). Due to their low cost, high photoactivity and stability, and non-toxic character, TiO_2 and ZnO are two among the most widely used semiconductors in PCO processes (Vikrant et al., 2019; Wang et al., 2021). In fact, ZnO showed better activity in PCO than TiO_2 for degradation of various pollutants, but due to its wide band gap energy (3.1–3.4 eV) and low separation of e^-/h^+ pairs, the application of pure ZnO in photocatalysis processes under visible light irradiation was limited (Ding et al., 2020). To address this concern, the formation of hetero-junction structures, including binary and ternary photocatalysts with suitable band gap energy, has been investigated in order to decrease the photo-generated charge carriers (Shi et al., 2018). By coupling various semiconductors, the band gap energy can be decreased and work at wide range of light.

The fabrication of metal and/or non-metal doped ZnO photocatalysts has been developed for improving the photoactivity of ZnO by introducing a new electronic state in the band structure of ZnO (Zhou et al., 2016). Furthermore, the presence of noble metals, such as Pt, Pd, Au and/or Ag NPs can enhance the photocatalytic performance of ZnO by surface modification (Lee et al., 2017; Chen et al., 2012; Luo et al., 2020). Due to their tunable physicochemical properties, NPs and bimetallic NPs have potential application in sensing, catalysis, photocatalysis and photonics. Ag is a noble NP with excellent features such as low cost, antibacterial properties and high electrical conductivity (Kohantorabi and Gholami, 2017). In photocatalytic applications, Ag NPs not only can induce a local surface plasmonic resonance effect, which can enhance the rate of reactions through the increase of local electromagnetic field, but also act as electron harvester that can enhance the light adsorption capability (Uen and Misawa, 2013; Xiao et al., 2016). Considering the above, a photo-catalyst that would combine the advantages of Ag, ZnO and $NiFe_2O_4$ could lead to a high efficacy and, to the best of the authors' knowledge is yet to be synthesized.

In the present study, we attempt to combine the previously described advantages and synthesize a MOF-based photocatalyst that will effectively activate PMS for the degradation of recalcitrant organic compounds. As such, we report a facile strategy for the successful synthesis of a mesoporous ZnO@$NiFe_2O_4$ nano-photocatalyst, starting from a MOF template (Fe_2Ni-MIL-88). The mesoporous catalyst with nanorod structure was fabricated through one-step annealing under air, which supposes a high efficacy in PMS activation and photocatalytic reaction. The mesoporous ZnO@$NiFe_2O_4$ catalyst is an ideal support for the immobilization of Ag NPs with high stability, and activity. The as-prepared catalyst (Ag/ZnO@$NiFe_2O_4$) was characterized by various techniques, and its efficacy on PMS activation was evaluated through a systematic assessment under different operational conditions (pH, catalyst/PMS ratio, matrix effect, etc.). Its photocatalytic performance was determined *via* the decomposition of Acetaminophen (ACT) in the presence of PMS as oxidant under UVA-LED irradiation. Finally, in order to assess the efficacy of PMS activation and identify the dominant pathways to ACT degradation, radical scavenging experiments were deployed, and the generated intermediates were followed *via* LC-MS analysis.

2. Materials and Methods

2.1. Chemicals and reagents

Iron chloride hexahydrate ($FeCl_3$. $6H_2O$), nickel nitrate hexahydrate (Ni $(NO_3)_2$. $6H_2O$), zinc acetate tetrahydrate (Zn $(CH_3COO)_2$. $4H_2O$), sodium borohydrate ($NaBH_4$), methanol (MeOH), ethanol (EtOH), ammonia solution (NH_4OH), dimethyl formamide (DMF) and acetonitrile were supplied from the Merck Co. Silver nitrate ($AgNO_3$), concentrated sulfuric acid (H_2SO_4), sodium hydroxide (NaOH), PMS (Oxone, $2KHSO_5.KHSO_4.K_2SO_4$), 2-hydroxy-1,4-benzenedicarboxylic acid (H_2BDC) and all scavengers, such as oxalate (OX), *p*-Benzoquinone (BQ), and *tert*-butyl alcohol (TBA) were obtained from Sigma-Aldrich Inc. All sodium salts including sodium chloride (NaCl), sodium sulfate (Na_2SO_4), sodium bicarbonate ($NaHCO_3$), sodium phosphate (Na_3PO_4), and sodium nitrate ($NaNO_3$) were purchased from Merck. Deionized (DI) water was used for all synthesis processes and treatment. HPLC grade water was obtained from Merck Co. The pure acetaminophen (ACT) powder for all the catalytic tests in this study was obtained from a local supplier (Aria Co, Iran). 0.65 g of ACT powder was dissolved in 1.0 L of water, stored at 4.0 ± 1 °C, and replaced regularly.

2.2. Analytical techniques

In order to study the phase purity and crystalline structure of the catalysts, X-ray diffraction (XRD) patterns were obtained on Philips X'Pert-MPD X-ray diffractometer with a Cu Kα radiation (λ = 1.54060 A°) in the 2Θ range of 10-80°. The surface morphologies and elemental analysis of catalysts were characterized by field emission scanning electron microscopy (FE-SEM, Mira3 Tascan), high-resolution transmission electron microscopy (HR-TEM, Philips-CM30 instrument) and energy dispersive X-ray spectroscopy (EDX), respectively. For identification of the surface composition of catalyst and binding energy of elements, X-ray photoelectron spectroscopy (XPS) analyses were carried out with a SPECS Phoibos 100 MCD5 hemispherical electron analyzer operating at a constant pass energy. K_α Mg (1253.6 eV) was the X-ray source employed together with a flood electron gun to compensate charge effects on the catalysts. Survey and high-resolution spectra were performed with an energy pass of 90 eV and step energy of 1.0 eV, and with an energy pass of 30 eV and step energy of 0.1 eV, respectively. The optical properties of the catalysts were examined through UV-Vis diffused reflectance spectroscopy (DRS, Shimadzu 2550-8030 spectrophotometer) in the wavelength range

of 200-600 nm. Also, the photoluminescence (PL) spectra were obtained *via* a FL3-TCSPC fluorescence spectrophotometer at room temperature. Electrochemical impedance spectroscopy (EIS) measurement was provided by using Na_2SO_4 solution (0.3 M) with frequency ranging between 0.1-10^6 Hz. The magnetic characteristics of the samples were determined by a vibrating sample magnetometer (VSM, PPMS). The solution pH was adjusted by using a Jenway pH-meter (Jenway Co. UK). Brunauer–Emmett–Teller (BET) analysis for the evaluation of specific surface area and pore size distribution was carried out on a Micromeritics/Gemini-2372 analyzer *via* N_2 adsorption/desorption at 77 K. In order to assess metal leaching after experimentation, the elemental analysis of the reaction solution was evaluated by inductively coupled plasma-atomic emission spectroscopy (ICP-AES) on a Varian 730-ES spectrophotometer. The concentration of ACT during the reaction was determined by high performance liquid chromatography (HPLC, Eclipse plus C18column; 3.5 μm, Agilent Co) equipped with a UV detector at 242 nm; the mobile phase was a mixture of acetonitrile and phosphate buffer (pH = 4.0) with a volumetric ratios 15:85, and injected with at a flow rate of 1.0 mL min^{-1}. Moreover, the total organic carbon (TOC) of the samples was analyzed by using Shimadzu TOC Analyzer (TOC-L CSH/CSN). The main intermediates produced during the photocatalytic degradation of ACT under the experimentally defined optimal conditions were determined by using liquid-chromatography-mass spectroscopy (LC-MS, 2010 A/Shimadzu) coupled with an Eclipse Atlantis T3, C18 column (2.1×100 mm, 3.0 μ particle size) at ambient temperature. The mobile phase of this analysis consisted of acetonitrile (containing 0.1% formic acid), and water (containing 0.1% formic acid), with injected flow rate 0.2 mL/min, and sample volume of 10.0 μL. Also, the following conditions were selected for the Mass spectrophotometer: gas nebulizer: nitrogen (N_2), capillary volt: 4.0 kV, Cone volt: 30 V, flow gas: 3.3 L/min, while source and desolation temperatures were 120 °C and 350 °C, respectively. The spectrophotometer scanning was collected for the 50-500 *m/z* range.

2.3. Synthesis of the Fe_2Ni-MIL-88 and $NiFe_2O_4$ nanorods

The Fe_2Ni-MIL-88 nanorods were synthesized by a previously verified hydrothermal method (Li et al., 2020). Briefly, 0.233 g (0.86 mmol) of $FeCl_3$. $6H_2O$, and 0.189 g (1.03 mmol) of Ni $(NO_3)_2$. $6H_2O$ were dissolved in 40 mL dimethyl formamide (DMF). Afterwards, 0.188 g (1.03 mmol) of H_2BDC was added into the above

solution under continuous stirring until a clear yellow solution was obtained (30 min). Then, 4.0 mL of NaOH solution (0.2 M) was poured into the above mixture and stirred for another 30 min. The obtained brown solution was transferred into a 50 mL Teflon-lined stainless-steel autoclave and heated at 100 ºC for 15 h. After cooling to room temperature, the products were collected by centrifugation, and washed three times with DMF and ethanol. Finally, the samples were dried at 70 ºC for 8 h. Following, the $NiFe_2O_4$ nanorods were prepared *via* calcination method. Fe_2Ni-MIL88 was placed in a muffle furnace and was heated at 450 ºC for 6 h with a heating rate of 2 ºC min^{-1} under air atmosphere.

2.4. Preparation of the mesoporous $ZnO_x@NiFe_2O_4$ nanorods (x = 0.02, 0.04, and 0.08)

0.124 g of as-synthesized Fe_2Ni-MIL88 nanorods were dispersed in 25 mL of DI water *via* ultrasonication. Then, 25 mL of Zn $(CH_3COO)_3$. $4H_2O$ solution (with different concentrations including 0.02 M, 0.04 M, and 0.08 M) was added dropwise into the suspension under stirring. The mixture was stirred at 500 rpm for 30 min at ambient temperature. Afterwards, the temperature of the solution was increased to 40 ºC and 20 mL of ammonia solution (5.0% v/v) was appended into the mixture. The mixture was stirred for 1 h until the reaction was completed. Then, the products were collected by centrifugation and washed with water. The dried products were annealed at 450 °C for 6 h with a heating rate of 2 ºC min^{-1}.

2.5. Synthesis of Ag NPs and decoration on the $ZnO_{0.04}@NiFe_2O_4$ nanorods

Ag NPs were decorated on the surface of $ZnO_{0.04}@NiFe_2O_4$ nanorod by using a reduction method. At first, 0.1 g of mesoporous $ZnO_{0.04}@NiFe_2O_4$ nanorod was dispersed in 20 mL of DI water by ultrasonication for 15 min. Then, 5.0 mL of silver nitrate ($AgNO_3$) solution (0.08 M) was added slowly into the suspension while the reaction was stirred at room temperature in the dark. After 30 min, 3.0 mL of $NaBH_4$ solution (0.05 M) was appended slowly into the mixture for the reduction of silver ions, while the solution color changed to black. The mixture was stirred for 1 h at room temperature until the reaction was completed. The obtained product (1.0 %w/w $Ag/ZnO_{0.04}@NiFe_2O_4$) was gathered *via* centrifugation and washed four times with water/ethanol, and finally dried at 70 ºC for 8h. In order to synthesize nanorods with various weight percentages of Ag NPs (3.0, and 5.0 %w/w), different amounts of silver nitrate solution were used during the preparation. Figure S1 (See

Supplementary Text ST1) summarizes the preparation processes of the mesoporous $Ag/ZnO_{0.04}@NiFe_2O_4$ nanorod catalyst applied in the present study.

2.6. Photo-catalytic evaluation of the synthesized catalysts

The catalytic performance of the as-made products including $NiFe_2O_4$, $ZnO_x@NiFe_2O_4$ (x = 0.02, 0.04, and 0.08), and $Ag/ZnO_{0.04}@NiFe_2O_4$ (Ag: 1.0, 3.0, and 5.0 %w/w) was evaluated against ACT degradation in the presence of PMS as oxidant under UVA irradiation. The working solution of ACT was prepared from a stock solution kept in at 4 ºC in a fridge. The photocatalytic reactions were carried out in a photo-reactor with a total volume of 50 mL. A quartz sheet was introduced on the top of the reactor, on which the LED setup was placed. The light intensity of LED setup was 228 $\mu W/cm^2$, and the distance between light source and reaction solution was 1.0 cm. The LED setup involved 19 light emitting diodes (Seoul Semiconductor, South Korea) which have emission wavelength of 365 nm (UVA), and assembled on an aluminum electrical board. In each experiment, a certain amount of catalyst was suspended into the 20 mL of ACT solution (12.0 mg/L, pH = 7.0) under ultrasonication. Then, 200 µL of PMS solution (20 mM) was appended into reaction, and the mixture was stirred under UVA irradiation. After various interval times (t = 2, 5, 8, 10, 12, and 15 min), 1.0 mL of reaction sample was taken, filtered by 0.22-µL PTFE membranes, and the removal of ACT was analyzed by HPLC. When the oxidant (PMS) was used in the reaction, after filtering the reaction solution, 200 µL of methanol was added to quench the radical species, and then the concentration of ACT was measured by HPLC. Moreover, control experiments by light, PMS, and catalyst alone were done under the same reaction conditions with a total time of 15 min. In order to study the effect of pH solution on ACT degradation reaction, the solution pH was adjusted by using NaOH, and H_2SO_4 (0.1 mM) solutions. It should be noted that, all experiments were performed at least in duplicate, and the obtained results are the average values, reported with their standard deviation (SD). The radical trapping experiments were carried out under identical conditions, in the presence of 50 mg/L scavenger including BQ, OX, TBA, and EtOH.

In order to study the stability and recyclability of the best performing catalyst, after each reaction the catalyst was separated from the media, washed several times with water/ethanol and then dried at 70 °C. The catalytic

performance was evaluated after four consecutive photo-catalytic cycles under the same reaction conditions (PMS addition and light).

2.7. Kinetic analysis

ACT degradation in the catalyst/PMS system under UVA irradiation was calculated by the eq. 1 as follows:

$$ACT\ degradation\ (\%) = \frac{ACT_0 - ACT_t}{ACT_0} \times 100 \quad (1)$$

Where, ACT_0 and ACT_t are the initial and final concentrations of ACT at time 0, and t, respectively. Moreover, the ACT mineralization was evaluated by using total organic carbon (TOC) measurements (eq. 2):

$$Mineralization\ (\%) = \frac{TOC_0 - TOC_t}{TOC_0} \times 100 \quad (2)$$

TOC_0 and TOC_t are the ACT concentrations at time zero and t during the photocatalytic reaction, respectively. In order to study the kinetics of ACT degradation in the presence of as-made catalysts, the pseudo-first order (PFO) reaction model was applied (eq. 3):

$$\ln\left(\frac{C_t}{C_0}\right) = -k_{app}.t \quad (3)$$

Where C_t, C_0, and k_{app} are the concentrations of ACT at time t, 0, and rate constant value, respectively. The k_{app} values were calculated form the slope of $\ln(\frac{C_t}{C_0})$ versus reaction time in all experiments. Also, the observed PFO rate (r_{obs}) of ACT degradation was determined from the eq.4, in which r_{obs} was reported in mg L^{-1} min.

$$r_{obs} = k_{app}C_0 \quad (4)$$

The quantum yield (QY) of photocatalytic system was calculated by using the following equation (eq. 5) (Reza et al., 2020). QY value is an effective factor for evaluation of photocatalytic performance.

$$Quantum\ yield = \frac{Decay\ rate\ (molecule\ per\ second)}{Photon\ flux\ (Photon\ per\ second)} \quad (5)$$

In order to meaning-fully evaluation of the photocatalytic activity, Figure of Merit (FoM) parameter was estimated by using equation 6 (Vikrant et al., 2019). As the FoM factor involved all the relevant performance variables, a good metric concerning the actual performance of an aqueous photocatalytic system can be obtained.

$$FoM = \frac{Conversion\ efficiency\ (\%)}{Catalyst\ mass\ (mg) \times [concentration]_0\ (ppm) \times Irradiation\ time\ (\text{min}) \times \text{Applied power (W)}} \quad (6)$$

3. Results and discussion

3.1. Catalyst characterization

In order to determine the crystalline structure and phase purity of the as-prepared catalysts including Fe_2Ni-MIL-88, $NiFe_2O_4$, $ZnO_{0.04}@NiFe_2O_4$, and $Ag/ZnO_{0.04}@NiFe_2O_4$ nanorod, XRD analysis was carried out and the obtained patterns are depicted in Fig. 1. The pure MOF (Fe_2Ni-MIL-88) shows strong peaks centered at 11.2°, 12.05°, 18.7°, 20.1°, and 23.4° which confirmed the formation of Fe_2Ni-MIL-88 nanorods *via* the employed hydrothermal method (Li et al., 2020). The characteristic peaks of $NiFe_2O_4$ nanorods were observed at 18.4°, 35.7°, 37.4°, 43.3°, 53.8°, 57.3°, 62.9°, and 74.6° that attributed to the (111), (311), (222), (400), (422), (511), (400), and (533) planes, respectively (JCPDS No. 54-0964) (Li et al., 2020). Based on these results, the $NiFe_2O_4$ nanorods were successfully synthesized by annealing at 450 °C under air, obtaining high crystallinity. By addition of the ZnO on the surface of $NiFe_2O_4$, two sharp peaks related to ZnO (marked with ♦ in Fig. 1) appeared at 2Θ = 37.1°, and 47.5° in the XRD pattern of $ZnO_{0.04}@NiFe_2O_4$ corresponding to the crystal planes of (101), and (102) hexagonal ZnO (JCPDS No. 36-1451), respectively (Zhou et al., 2016). The diffraction peak of the ZnO structure at 37.1 degree has an overlap with the XRD peak of $NiFe_2O_4$ (2Θ = 37.4°), for this reason in the XRD patterns of $ZnO_{0.04}@NiFe_2O_4$ and $Ag/ZnO_{0.04}@NiFe_2O_4$ nanorod the intensity of this peak increased, compared to pure $NiFe_2O_4$, and confirmed the presence of ZnO in the as-made catalysts. Due to the low ratio and low proportion in the sample, the characteristic peaks of ZnO in the XRD patterns of $ZnO_{0.04}@NiFe_2O_4$, and $Ag/ZnO_{0.04}@NiFe_2O_4$ nanorods cannot be clearly separated. In order to verify the ZnO presence, we confirmed it by the HR-TEM, and EDX analysis, in the following part of catalyst characterization (*vide infra*). Finally, for the $Ag/ZnO_{0.04}@NiFe_2O_4$ catalyst, three additional characteristic peaks were observed at 44.4°, 66.2°, and 78.5° which are related to the (200), (220), and (311) planes of cubic structure of Ag NPs, respectively (JCPDS No. 01-087-0720) (Xiao et al., 2016). According to the literature, Ag can be incorporated into the ZnO lattice as interstitial atoms or as a substituent for Zn^{2+} (Khavar et al., 2019).

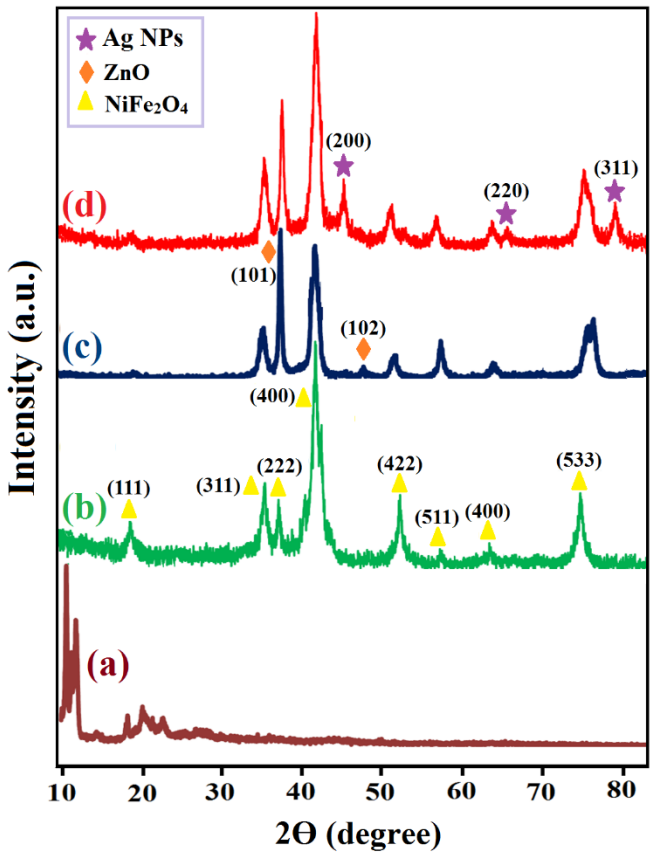

Figure 1. XRD patterns of Fe_2Ni-MIL-88 (a), $NiFe_2O_4$ (b), $ZnO_{0.04}$@$NiFe_2O_4$ (c), and 1.0% w/w Ag/$ZnO_{0.04}$@$NiFe_2O_4$ nanocomposite (d).

In order to study the morphology of the samples, FE-SEM, and HR-TEM analysis were applied. As shown in Fig. 2a and 2b, the as-prepared Fe_2Ni-MIL-88 nanorods have an average length around 580 nm, outer diameters in the range of 100 nm, and were distributed without agglomeration. According to the FE-SEM images of the $NiFe_2O_4$ nanorods, the diameter of this nanostructure was decreased (60.0 nm) compared to Fe_2Ni-MIL-88, due to the removal of the organic linkers and compounds, through the calcination of the Fe_2Ni-MIL-88 template. In addition, the mesoporous property of the sample after calcination was observed from the FE-SEM images (Fig. 2c and 2d). As shown in Fig. 2d, due to the presence of the ZnO in the $ZnO_{0.04}$@$NiFe_2O_4$, the nanorod length was increased and reached around 615 nm.

Following, details on the morphology of the sample were acquired by HR-TEM analysis (Fig. 2e-h). A close observation of the $ZnO_{0.04}$@$NiFe_2O_4$ catalyst shows the nanorod structure (Fig. 2e). Due to the higher mass thickness, in contrast to the as-made catalyst, the $NiFe_2O_4$ is black and the ZnO has a bright color in these

images. The thickness of the ZnO on the top and/or bottom of the $NiFe_2O_4$ in the as-prepared catalyst was around 40-60 nm. These results are in good agreement with FE-SEM images, which indicated that the length of $ZnO_{0.04}@NiFe_2O_4$ structure was higher than that of pure $NiFe_2O_4$ and confirmed the formation of ZnO on $NiFe_2O_4$. Moreover, the results obtained by HR-TEM verified that the $NiFe_2O_4$ with a mesoporous structure has been achieved by the annealing process. According to Fig. 2g and 2h, the interplanar spacing of 0.282 nm, and 0.275 nm seen in the HR-TEM images are related to the (311), and (101) planes of $NiFe_2O_4$ and ZnO in as-made mesoporous nanorod, respectively. Based on the above results, the $ZnO_{0.04}@NiFe_2O_4$ catalyst was successfully synthesized by the reported method.

As presented in Fig. 2i through 2m, oxygen (O), iron (Fe), nickel (Ni), zinc (Zn), and silver (Ag) were distributed uniformly in as-prepared sample, and suggested that the ZnO and Ag NPs were successfully synthesized, and loaded on the surface of $NiFe_2O_4$ nanorods. Moreover, the EDX spectrum of 1.0% w/w $Ag/ZnO_{0.04}@NiFe_2O_4$ nanorod proved the presence of O, Fe, Ni, Zn, and Ag within the nanorod (Fig. 2n). Due to the synthesis of $NiFe_2O_4$ from the calcination of Fe_2Ni-MIL-88, the presence of carbon can be related to the MOF support. No other elements were observed in the EDX spectrum of sample, which indicated the high purity of as-made nanocomposite. Based on the EDX spectrum, the amount of Ag in the as-made catalyst was obtained to be 1.02 % w/w as intended in the synthesis section.

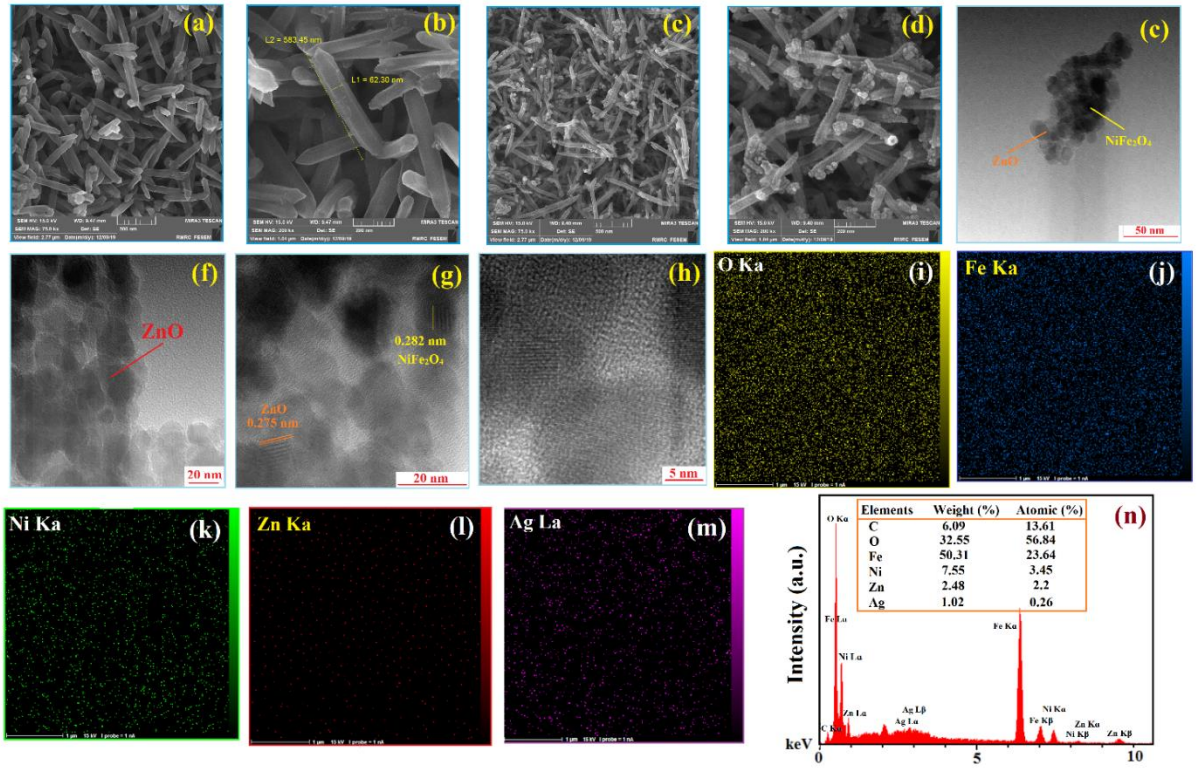

Figure 2. FE-SEM images of Fe_2Ni-MIL-88 (a, and b), $NiFe_2O_4$ nanorods (c), and $ZnO_{0.04}$@$NiFe_2O_4$ (d), HR-TEM images of $ZnO_{0.04}$@$NiFe_2O_4$ nanorod (e-h), elemental mapping of oxygen (i), iron (j), nickel (k), zinc (l), and silver (m), and EDX spectrum of mesoporous 1.0% w/w Ag/$ZnO_{0.04}$@$NiFe_2O_4$ nanorod (n).

In order to identify the valence state of the various species contained in the as-made catalyst, XPS measurements were performed. The XPS survey spectra of the 1.0% w/w Ag/$ZnO_{0.04}$@$NiFe_2O_4$ nanorod was illustrated in Fig. 3a. The results indicated the presence of Ni, Fe, O, Zn, and Ag in the catalyst composition. Moreover, high-resolution spectra of Ni 2p, Fe 2p, O 1s, Zn 2p, and Ag 3d are depicted in Fig. 3b-f. The deconvolution of the Ni 2p exhibited four peaks (Fig. 3b). The peaks at binding energies of 854.7 eV and 872.3 eV corresponded to Ni $2p_{3/2}$ and Ni $2p_{1/2}$ orbitals, respectively, and the satellite peaks (shake-up type peaks) at higher energies than that of the main peaks (Ni $2p_{3/2}$: 860.4 eV and Ni $2p_{1/2}$: 877.6 eV). Both the main and satellite peaks proved that the oxidation state of Ni cation is +2 (Fu et al., 2013, Jin et al., 2013) in the 1.0% w/w Ag/$ZnO_{0.04}$@$NiFe_2O_4$ nanorod. Regarding the Fe 2p spectrum, the deconvolution of the Fe $2p_{3/2}$ showed the existence of three main peaks at 709.6 eV, 711.1 eV and 713.1 eV and the satellite peak at 718.0 eV. The peak at 709.6 and 711.1 eV can be assigned to Fe^{3+} cations located octahedral and tetrahedral sites, respectively, and the peak at 713.1 eV

can be corresponded to Fe^{3+} cations at the surface of $NiFe_2O_4$ bonded to hydroxyl and carboxylate groups (Moulder et al., 1992). Besides, two peaks located at 723.7 eV and 725.6 eV are associated with Fe $2p_{1/2}$. These peaks can be attributed to Fe^{3+} species (Xu et al., 2019). The deconvolution of O 1s spectra confirmed the presence of three peaks at 529.7 eV, 531.2 eV and 532.7 eV (Fig. 3d). The first peak was attributed to O^{2-} ions in the M-O bonding {M= Ni^{2+}, Fe^{3+}, and Zn^{2+}} of the $ZnO_{0.04}$@$NiFe_2O_4$. The second and third peaks were ascribed to M-OH bonding and the presence of C=O bonding originated from the acetate molecules adsorbed onto the catalyst surface, respectively (Zhou et al., 2019, Ortiz-Quiñonez et al., 2018). The surface hydroxyl group (—OH) has a critical role in generation of ROS especially $HO^{\bullet}$ and $O_2^{\bullet-}$, through capturing of photo-generated electrons, which can enhance the reaction efficiency (Zhou et al., 2016). Considering the Zn 2p spectrum (Fig. 3e), the fitting of two peaks located at 1021.4 eV and 1044.4 eV can be associated with Zn $2p_{3/2}$ and Zn $2p_{1/2}$, respectively (Al-Gaashani et al., 2013). These peaks are related to the zinc lattice in ZnO (Van Khai et al., 2016). The peak separation between $2p_{3/2}$ and $2p_{1/2}$ orbitals is 23 eV, which is in agreement with the reference value of ZnO (Al-Gaashani et al., 2013). These results indicated that the valence state of Zn on the surface of the 1.0% w/w Ag/$ZnO_{0.04}$@$NiFe_2O_4$ nanorod is +2. In the case of Ag spectrum (Fig. 3f), two peaks at binding energies of 368.0 eV and 374.0 eV were identified. These peaks were attributed to Ag $3d_{5/2}$ and Ag $3d_{3/2}$, respectively, and are characteristic of metallic Ag (Zou et al., 2019; Potlog et al., 2015). Therefore, the oxidation state of Ag in the nanorod is 0. The summary of the XPS analysis of the 1.0% w/w Ag/$ZnO_{0.04}$@$NiFe_2O_4$ nanocomposite is shown in further detail at Table S1.

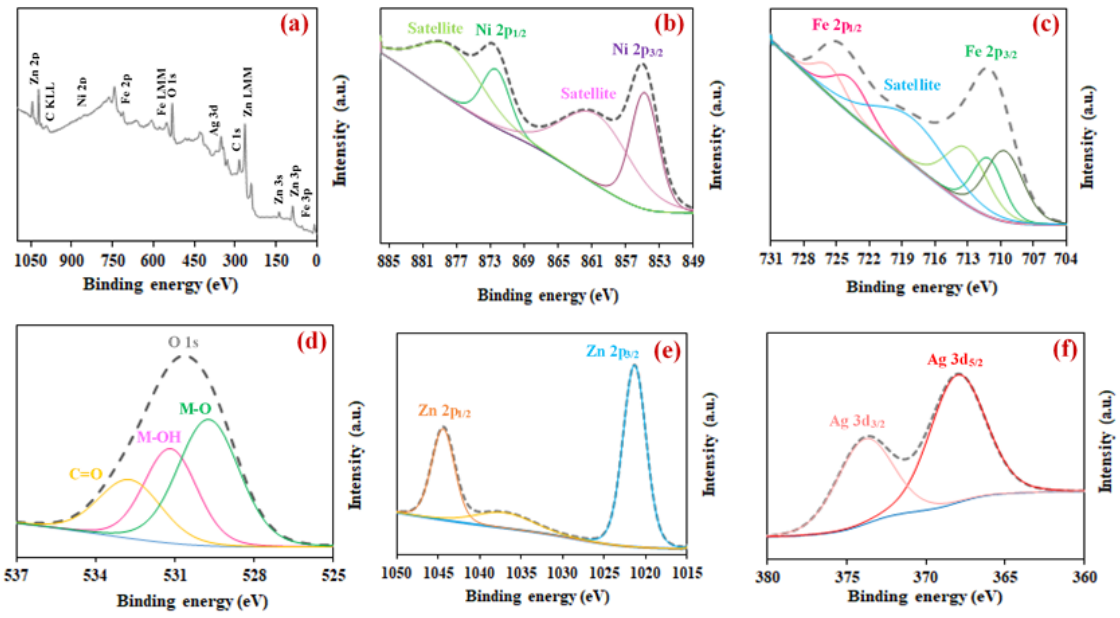

Figure 3. XPS survey spectra of 1.0% w/w Ag/$ZnO_{0.04}$@$NiFe_2O_4$ nanocomposite (a), and the high-resolution spectra of Ni 2p (b), Fe 2p (c), O 1s (d), Zn 2p (e), and Ag 3d (f) (M = Ni^{2+}, Fe^{3+}, and Zn^{2+}).

The optical properties of the samples were investigated by UV-Vis DRS and photoluminescence (PL) analysis at room temperature. Also, the role of Ag NPs on the possible change in band gap energies was studied. The optical band gap energies of samples were calculated from the absorption data by Tauc/David-Matt model (eq. 7).

$$(Ahv) = \alpha\,(hv - E_g)^{n/2} \quad (7)$$

Where A, *h*, *v*, *a*, and E_g are the constant value, Plank's constant, light frequency, absorption coefficient, and band gap energy, respectively (Low et al., 2014). In this equation, the value of n is dependent to the direct/indirect transition, which can give 1 and 4 values in the presence of direct and indirect transitions, respectively (Salari and Kohantorabi, 2020). The optical band gap energy was calculated from the slope of $(ahv)^2$ versus *hv* (eV) plot. Fig. 4a depicts the UV-Vis DRS spectra of $NiFe_2O_4$, $ZnO_{0.04}$@$NiFe_2O_4$ and 1.0% w/w Ag/$ZnO_{0.04}$@$NiFe_2O_4$ nanorod. By loading ZnO onto the $NiFe_2O_4$ and Ag NPs on the surface of $ZnO_{0.04}$@$NiFe_2O_4$, the adsorption edge of the synthesized nanorod was not shifted. In addition, all samples have similar adsorption edges (Fig. 4a), which reveals that the ZnO and Ag NPs did not have an effect on band gap width of $NiFe_2O_4$. In the presence of the Ag NPs in the as-made nanorod, the adsorption background was improved, and confirmed the role of these NPs on adsorption light that is related to the blackbody effect of Ag NPs (Kohantorabi et al., 2021b). According to the obtained results from Fig. 4b, the approximate E_g of $NiFe_2O_4$, $ZnO_{0.04}$@$NiFe_2O_4$ and 1.0% w/w Ag/$ZnO_{0.04}$@$NiFe_2O_4$ nanorods was calculated to be 1.88, 2.05, and 1.87 eV, respectively.

The photoluminescence (PL) spectra of the as-prepared catalysts after excitation are exhibited in Fig. 4c. The surface properties have a vital role in the luminescence characteristic peak of the samples. According to the obtained spectra, the luminous intensity of the samples was observed at 359.0 nm that is attributed to the green emission of the as-synthesized nanorods. All catalysts showed similar PL spectra, but with different intensities. Based on the results, the PL intensity of $NiFe_2O_4$ decreased by the insertion of ZnO and Ag NPs. Due to the presence of Ag NPs as a noble metal in as-made nanocomposite, the recombination rate of photo-generated

charge careers was changed. The presence of Ag NPs in the catalyst, not only can improve the separation efficiency of the photo-generated e^-/h^+, but also enhance the light absorption capacity. Moreover, the Ag NPs can act as electron traps for the photo-generated electron from the conduction band (CB) of ZnO and enhance the separation of photo-generated charge carriers. Based on the above results, the as-prepared ternary nanocomposite is expected to show higher photocatalytic performance compared to pure $NiFe_2O_4$ and the binary nanorod ($ZnO_{0.04}$@$NiFe_2O_4$), due to their e^-/h^+ separation ability and faster charge carrier transport.

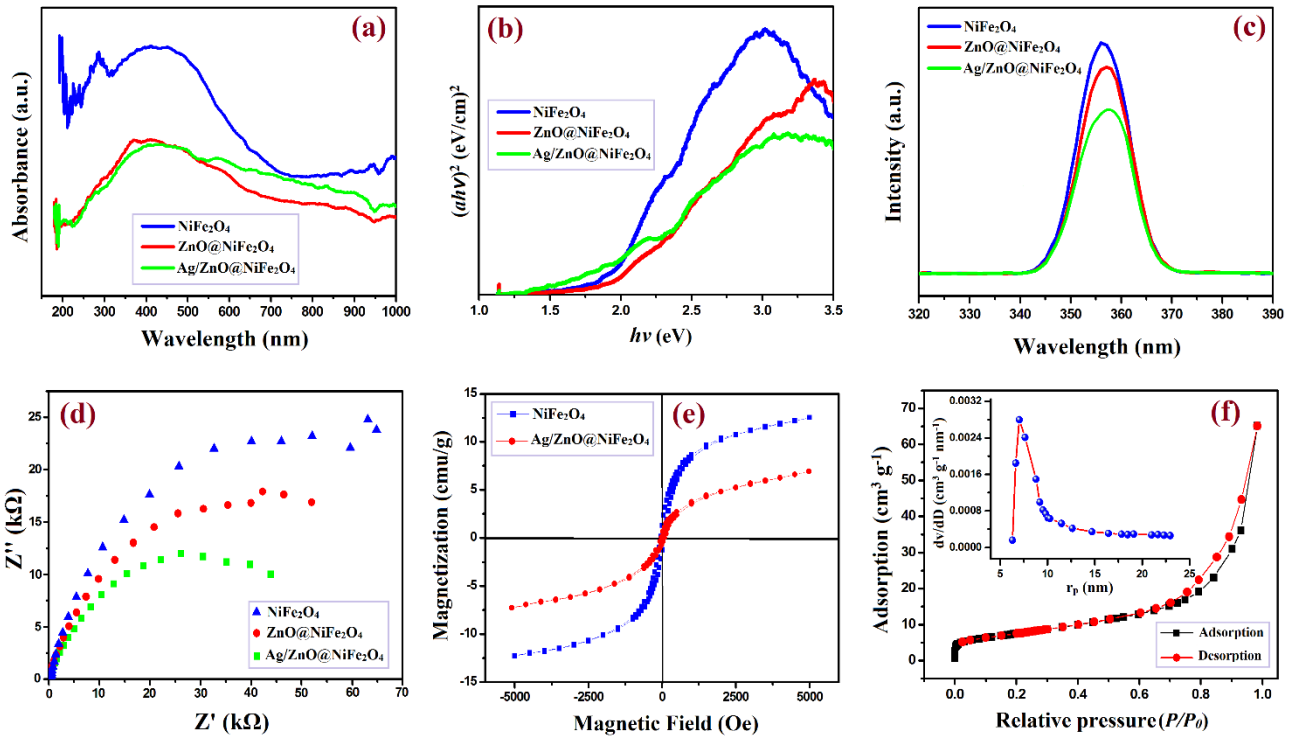

Figure 4. (a) UV-Vis diffuse reflectance spectra, (b) Tauc's plots, (c) photoluminescence (PL) spectra, (d) Impedance Nyquist plots at OCP voltage of as-prepared $NiFe_2O_4$, $ZnO_{0.04}$@$NiFe_2O_4$, and 1.0% w/w Ag/$ZnO_{0.04}$@$NiFe_2O_4$ catalysts, (e) VSM analysis of $NiFe_2O_4$, and 1.0% w/w Ag/$ZnO_{0.04}$@$NiFe_2O_4$ nanorod, and (f) N_2 adsorption/desorption isotherms of 1.0% w/w Ag/$ZnO_{0.04}$@$NiFe_2O_4$ at 77 K.

In order to evaluate the charge transport role of ZnO and Ag NPs on the photocatalytic performance of $NiFe_2O_4$, Electrochemical Impedance measurements (EIS) was performed. Figure 4d shows the Nyquist plots of $NiFe_2O_4$, $ZnO_{0.04}$@$NiFe_2O_4$, and 1.0% w/w Ag/$ZnO_{0.04}$@$NiFe_2O_4$ under UVA-LED. Based on the EIS results, the presence of Ag NPs could accelerate the electron charge transfer rate, which is expected to enhance the

photocatalytic performance. As observed in Fig. 4d, by introducing the ZnO and then Ag NPs, the impedance arc radius of the catalyst decreased that confirmed the efficient separation of charge carriers.

Furthermore, magnetism is a vital property of catalysts, when it comes to potential environmental applications. The room-temperature magnetic behavior of the as-made samples including $NiFe_2O_4$, and 1.0% w/w $Ag/ZnO_{0.04}@NiFe_2O_4$ was determined by using vibrating sample magnetometer (VSM). The obtained results were depicted in Fig. 4e. The saturation magnetization (M_S) values of $NiFe_2O_4$ was around 12.20 emu g^{-1}. After coating NiFe2O4 with ZnO and then Ag NPs, this value was decreased and reached to be 7.30 emu g^{-1}. Due to the interaction between ligands and the ZnO layer on the surface of support, the magnetic property of as-made nanocomposite was reduced.

Also, the mesoporous structure of the as-made sample was confirmed by using N_2 adsorption/desorption isotherms, reported in Fig. 4f. According to isotherm of sample, due to the presence of a hysteresis loop at ($0 < P/P_0 < 1$), the catalyst can be related to the type IV. In catalytic and photocatalytic reactions, the surface area is an important parameter which can enhance the final activity. The specific surface area and the average pore size of 1.0% w/w $Ag/ZnO_{0.04}@NiFe_2O_4$ nanorod was calculated to be 25.01 m^2 g^{-1}, and 6.98 nm, respectively. These results indicated that the as-prepared catalyst has a mesoporous structure (6.3-10.0 nm), as it can be seen from the insert in Fig.4f, which is in good agreement with HR-TEM results. Nevertheless, we need to underline that the photoactivity of any catalyst does not only depend on the surface area, but also related to the light absorption ability especially metal nanoparticles which can enhance the separation of charge carriers (Pan and Xu, 2013).

3.2. Evaluating the PMS-enhanced photo-catalytic activity of the synthesized materials by assessing ACT degradation

3.2.1. Effect of the Zn^{2+} solution concentration during synthesis of the $ZnO@NiFe_2O_4$ nanorods

As a first step of the evaluation of the (photo)catalytic and PMS activation capacity of our composite, we studied the effect of the Zn^{2+} solution concentration during the synthesis of ZnO on $NiFe_2O_4$ and its effect on UVA-mediated photocatalytic activity, peroxymonosulfate (PMS) activation and combined UVA/PMS photocatalytic activation, evaluated by ACT degradation. For this purpose, different concentrations of zinc ions including 0.02, 0.04, and 0.08 M were used during the synthesis process (as described in Section 2.4). The obtained results

were summarized and are reported in Fig. 5a. The adsorption of ACT on the surface of catalyst increased from 18.6% to 29.1%, when the concentration of zinc solution was increased from 0.02 to 0.04 M during the synthesis process. Furthermore, the concentration of zinc solution in synthesis process of ZnO has a negligible effect on ACT photocatalytic decomposition under UVA light. By addition of PMS as an oxidant during the reaction, the ACT removal efficiency was increased and reached 74.8%, which indicated the high potential of the as-made nanocomposite in PMS activation (Fig. 5a). In fact, due to the presence of Fe^{3+}, and Ni^{2+} in the as-made sample, PMS can be activated and generate $HO^{\bullet}$ and $SO_4^{\bullet-}$. When the UVA/PMS process was coupled with the various as-made catalysts, the removal efficiency of ACT was as follows: ZnO@$NiFe_2O_4$ (93.6%) > ZnO@$NiFe_2O_4$ (90.05%) > ZnO@$NiFe_2O_4$ (73.0%) while 0.04 M, 0.08 M, and 0.02 M of zinc solution was used in synthesis route, respectively. These results indicated the high ability of the binary catalysts on UVA-assisted PMS activation process. Summarizing, based on the above results, the ZnO@$NiFe_2O_4$ nanorod which was prepared in the presence of 0.04 M of zinc solution showed the best photocatalytic performance in PMS activation, and 93.6% ACT removal was observed during 15.0 min by coupling with UVA/PMS process.

In order to study the kinetics of reaction by using these processes, the PFO rate constants were determined, and reported in Fig. S2a. These values were calculated to be 0.065 min^{-1}, and 0.087 min^{-1} for the $NiFe_2O_4$/UVA/PMS, and $ZnO_{0.02}$@$NiFe_2O_4$/UVA/PMS processes, respectively from the slope of ln (C_t/C_0)-time (see Supplementary Text ST3). Although it should be noted that by increasing the concentration of zinc solution to 0.04 and 0.08 M during the synthesis of ZnO on $NiFe_2O_4$, the PFO rate constant values for catalyst/UVA/PMS processes were 2.74, and 2.35 times higher than $NiFe_2O_4$/UVA/PMS, indicating the important role of ZnO in photocatalytic PMS activation.

3.2.2. Effect of Ag dosage on the catalytic activity of ZnO@$NiFe_2O_4$ nanorod

In order to assess the effect of Ag on the catalytic activity, different values (1.0%, 3.0%, and 5.0% w/w) of Ag NPs were anchored on the surface of $ZnO_{0.04}$@$NiFe_2O_4$ nanocomposite. Fig. S2b shows that in presence of 1.0%w of Ag NPs, the removal efficiency was increased from 93.6% in Ag-free sample, and reached 100% within 15 min. By addition of Ag weight percent up to 3.0%, and 5.0% w, the ACT removal decreased slightly, at 98.0%, and 96.8%, respectively. The PFO rate constants (k_{app}) of ACT degradation in the presence of these

samples were calculated and shown in Fig. 5b. Although the ACT removal efficiency was not significantly changed in the presence of various values of Ag NPs (including 1.0%, 3.0%, and 5% w/w on the surface of $ZnO_{0.04}$@$NiFe_2O_4$ catalyst), we report that the k_{app} values were calculated to be 0.368 min^{-1}, 0.24 min^{-1}, and 0.22 min^{-1}, respectively, which are 2.07, 1.35, and 1.24 times higher than calculated value in the Ag-free $ZnO_{0.04}$@$NiFe_2O_4$ nanorod (0.178 min^{-1}). These results confirmed the critical role of Ag NPs in the as-made nanocomposite for the enhancement of photocatalytic activity of samples.

Compared with plain $NiFe_2O_4$ nanorods, where only 62.2% of ACT removal was observed in $NiFe_2O_4$/UVA/PMS process, the addition of the ZnO and Ag NPs improved the photocatalytic activity of sample, not only by reducing the recombination rate of the photo-generated e^-/h^+ but also by improvement of the activation rate of PMS for the generation of radical species. Based on the above results, we note that Ag NPs can enhance the light harvesting and reduce the charge carrier recombination rate of the photocatalytic process. From here onwards, the Ag/ZnO@$NiFe_2O_4$ nanorod with 0.04 M of Zn solution for the preparation of the ZnO and 1.0% w of Ag NPs was selected as optimum catalyst loading for the next experiments in the present study. As such, in order to enhance the performance of reaction, a suitable activator is needed. At constant concentration of PMS (0.2 mM), different values of catalyst were selected (For more details, see Supplementary Text ST4). Hence, the ratio of catalyst:PMS 0.5 g/L. mM was chosen as optimum value for the 1.0% w/w Ag/$ZnO_{0.04}$@$NiFe_2O_4$ nanocomposite (Fig. S4).

3.2.3. Catalytic potential of the synthesized Ag/ZnO@$NiFe_2O_4$ nanorod in PMS activation

Fig. 5c illustrates the ACT removal during the photocatalytic PMS activation in the different processes under the same reaction conditions ([ACT] = 12.0 mg/L, and [PMS] = 0.2 mM, under UVA). The ACT removal in blank experiment only by UVA and $NiFe_2O_4$ nanorods were around 2.40%, and 8.50%, respectively, indicating that the direct photolysis of ACT is negligible by the UVA. Also, in the presence of PMS as oxidant without activation, 18.8% of ACT was removed from the reaction media, while by adding the UVA into the system the ACT removal efficiency was enhanced and reached to the 38.15%, and k_{app} around 0.024 min^{-1}. This result corroborates with other works that indicate a PMS activation by UVA light (Ghanbari et al., 2019; Guan et al., 2011; Ozores-Diez et al. 2020).

Continuing with further control experiments, by addition of PMS into the reaction medium containing $NiFe_2O_4$ nanorods as a catalyst, the ACT removal efficiency was increased and reached 55.5%, indicating an important activation of PMS by Fe and Ni from the structure of the catalyst, owing to the generation of $HO^{\bullet}$ and $SO_4^{\bullet-}$. The reversible cycling between various valence states of metals is very important factor for generation of further active radicals. The Fe^{3+} sites on the surface of $NiFe_2O_4$ can activate the PMS to $SO_5^{\bullet-}$, and $SO_4^{\bullet-}$ (Ghanbari et al., 2019). Two main reactions can be occurred in the $NiFe_2O_4$/PMS system as following (eqns. 8, and 9):

$$HSO_5^- + Fe^{3+} \longrightarrow Fe^{2+} + SO_5^{\bullet-} + H^+ \qquad k = Not\ found \qquad (8)$$

$$HSO_5^- + Fe^{2+} \longrightarrow Fe^{3+} + SO_4^{\bullet-} + HO^- \qquad k = 3.0 \times 10^4\ M^{-1}s^{-1} \qquad (9)$$

In contrast to the high activity of the $NiFe_2O_4$ nanorods as a catalyst, only 18.4% of ACT could be removed in the $NiFe_2O_4$/UVA process, which shows a modest photo-catalytic potential, or the presence of a photo-induced metal leaching in the medium and induction of homogeneous PMS activation. According to obtained results, by introducing the PMS to system ($NiFe_2O_4$/UVA/PMS), 62.2% of ACT was removed, indicating the role of $NiFe_2O_4$ in activation of PMS. By addition of $NiFe_2O_4$ into the reaction system, H_2O would be physically adsorbed on the Ni^{2+} sites of $NiFe_2O_4$ and created Ni^{2+}-HO^- species. These species can react with PMS and generate $SO_4^{\bullet-}$ *via* the H-bond (eq. 10). It should be noted that the Ni^{2+}-HO^- species can be regenerated by the combination of the Ni^{3+}-HO^- species with HSO_5^- (eq. 11). Moreover, Ni^{2+} sites on the surface of catalyst can react directly with PMS, and generate the $HO^{\bullet}$ (eq. 12). This reaction increases the catalytic efficiency due to generation of $SO_4^{\bullet-}$, and $HO^{\bullet}$ (Xu et al., 2020b).

$$Ni^{2+} - HO^- + HSO_5^- \longrightarrow Ni^{3+} - HO^- + SO_4^{\bullet-} + HO^- \qquad (10)$$

$$Ni^{3+} - HO^- + HSO_5^- \longrightarrow Ni^{2+} - HO^- + SO_5^{\bullet-} + H^+ \qquad (11)$$

$$Ni^{2+} + HSO_5^- \longrightarrow Ni^{3+} + SO_4^{2-} + HO^{\bullet} \qquad (12)$$

Accordingly, the improvement of the photocatalytic activity of $NiFe_2O_4$ nanorods under UVA light when ZnO was synthesized on the surface of $NiFe_2O_4$ was assessed. As it can be seen from Fig. 5c, by this coating the ACT removal was increased and reached to be 93.6% in the $ZnO_{0.04}$@$NiFe_2O_4$/UVA/PMS system. This result confirmed the synergistic effect between the $NiFe_2O_4$ and ZnO in the as-made catalyst, for UVA-assisted PMS activation. By introducing ZnO, the photocatalytic efficiency was enhanced by the transformation of

electron/holes (e^-/h^+) pairs between ZnO and $NiFe_2O_4$. Moreover, a previous study reported that PMS can be activated by ZnO to generate $HO^\bullet$, and $SO_5^{\bullet-}$ (eq. 13) (Shukla et al., 2010).

$$ZnO + HSO_5^- \longrightarrow Zn^{2+} + HO^\bullet + SO_5^{\bullet-} \quad (13)$$

Finally, in the presence of Ag NPs as a noble metal on the surface of catalyst, the complete removal of ACT from the reaction media was obtained within 15 min. The catalyst demonstrated superior catalytic properties that can increase the light harvesting *via* surface plasmonic resonance, high ACT removal was observed in the 1.0% w/w $Ag/ZnO_{0.04}@NiFe_2O_4$/LED/PMS system.

In order to further understand the ACT degradation under the various studied systems, the k_{app} of each reaction was calculated and the results are reported in Fig. 5c. The values of k_{app} in ACT degradation under the UVA /PMS process increased in the following order: $NiFe_2O_4$ (0.065 min^{-1}) < $ZnO_{0.04}@NiFe_2O_4$ (0.178 min^{-1}) < 1.0% w/w $Ag/ZnO_{0.04}@NiFe_2O_4$ (0.368 min^{-1}). This means that the rate constant value of reaction in the 1.0% w/w $Ag/ZnO_{0.04}@NiFe_2O_4$/UVA/PMS process was 2.07 times higher than in the same system in absence of Ag NPs, and highlights that the presence of Ag NPs, enhances the harvesting of light that cause the high photocatalytic activity.

Based on the aforementioned results and the band gap data discussed in Section 3.1, by the synthesis of ZnO on $NiFe_2O_4$, and Ag NPs on the surface of nanocomposite, the band gap energies were changed slightly. The prepared nanorod can be activated by light (UVA), and due to the presence of transition metal such as Fe^{3+}, and Ni^{2+}, which can activate PMS to generate radicals, showed the best activity in ACT oxidation reaction. In order to contextualize our findings, the activity of our synthesized samples was compared with other catalytic/photocatalytic AOPs for ACT degradation reported in literature, and the obtained results are reported in Table S2. As deduced from the results, the catalyst/oxidant ratio in this study was found to be 0.5 g/L. mM which is lower than other reported works for ACT degradation catalyzed by Fe_3O_4 (Tan et al., 2014), and $MnFe_2O_4$ (Tan et al., 2017). Moreover, the r_{obs} (mg/L. min) values for the present study (4.42 mg/L. min) is higher than the reported values for similar processes and confirmed the high catalytic performance of as-prepared mesoporous catalyst (Noorisepehr et al., 2019). In comparison with other reported metal oxides, radical pathway ($SO_4^{\bullet-}$and $HO^\bullet$) is the dominant one for these systems, while non-radical pathway of ACT degradation was detected in the presence of Mn-g-C_3N_4 (Fan et al., 2019) and CoAl-layer double hydroxide

(CoAl-LDH) (Zhu et al., 2019). Our reported system apparently generates a high number of photo-produced reactive intermediates during the UVA assisted PMS activation and enhance the reaction efficiency compared to different sulfate radical based AOPs; a detailed analysis of these species is shown in a next section. Also, the mineralization of ACT during the photo-catalytic activation of PMS was investigated at the experimentally defined "optimum" conditions. The complete removal of ACT (12.0 mg/L) was obtained within 15 min, but the TOC removal was around 25%, while 63.0% mineralization occurred in 60 min. Due to the formation of structures resistant to oxidation, such as linear compounds, the TOC removal showed a lower, but still important rate.

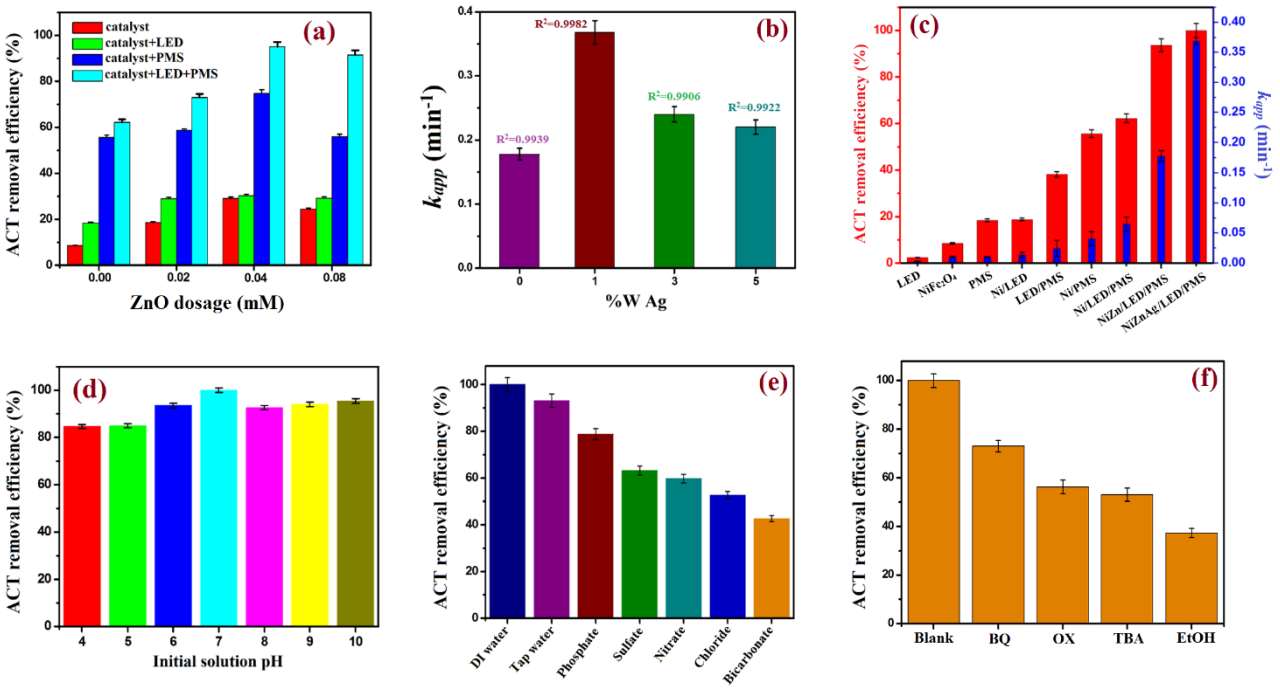

Figure 5. (a) Effect of ZnO dosage on catalytic activity of ZnO@$NiFe_2O_4$, (b) k_{app} values of photocatalytic degradation of ACT in the presence of different Ag percentages, and (c) removal of ACT, and calculated k_{app} values in different processes. (d) Effect of initial solution pH, (e) ions matrix, and (f) different scavengers on photocatalytic degradation of ACT. (Reaction conditions: [ACT] = 12.0 mg/L, [Catalyst] = 0.1 g/L, [PMS] = 0.2 mM, and reaction time = 15 min).

3.3. Operational parameters affecting the photo-catalytic activation of PMS and ACT degradation

3.3.1. Effect of initial solution pH

In order to study the effect of solution pH on the efficacy of the 1.0% w/w Ag/$ZnO_{0.04}$@$NiFe_2O_4$/UVA/PMS system, the reaction was carried out at different pH values (4.0–10) under the same reaction conditions. As it can be seen from the results (Fig. 5d), ACT degradation was not affected considerably by the solution pH. The maximum removal efficiency of ACT over the catalyst/UVA/PMS system was obtained at neutral pH (pH = 7.0). Also, the role of solution pH in the selected reaction can affect the surface charge of the catalyst and the speciation of PMS (Fanaei et al., 2019). Considering the former, the 1.0% w/w Ag/$ZnO_{0.04}$@$NiFe_2O_4$ catalyst has zero point charge pH (pH_{zpc}) around 8.7, which indicates that the as-made catalyst has positive surface at the pH value below 8.7. Based on the above results, and as can be seen from the Fig. 5d, the highest ACT removal was obtained at pH = 6.0 and 7.0, because the photocatalytic processes can occur either on or near the surface of the catalyst. However, the weak adsorption of ACT on the surface of 1.0% w/w Ag/$ZnO_{0.04}$@$NiFe_2O_4$ photocatalyst at natural pH (in secondary pH of 8.20) indicated that the reaction occurred in the vicinity of the catalyst.

According to the results, at high pH value (pH > 7.0) the ACT removal efficiency was not changed compared with the optimum condition (pH = 7.0). These values were obtained to be 92.60%, 93.54%, and 95.37%when the pH values are 8.0, 9.0, and 10, respectively. This behavior can be related to the generation of $HO^{\bullet}$ according to the equation 14. In addition, at high pH values (pH > pH_{zpc}) the surface charge of catalyst is negative. This property can affect the adsorption of PMS on the surface of catalyst, and subsequently, the reaction efficiency.

$$h^+ + HO^- \longrightarrow HO^{\bullet} \quad (14)$$

Moreover, at acidic media, due to the presence of H^+, the activation of PMS decreases, the electrostatic repulsion between the catalyst and ACT increases, and overall, a lower reaction efficiency was obtained. According to the pK_a value of PMS ($pK_{a2} = 9.4$), at natural and pHs below 9.4, HSO_5^- ions are the main species of PMS in water, meanwhile at solution pH over 9.4, SO_5^{2-} would dominate the reaction (Kohantorabi et al., 2021b). At pH lower than 9.4, the HSO_5^- ions can be attracted on the positive surface of catalyst and enhance the reaction efficiency by the generation of $SO_4^{\bullet-}$, and $HO^{\bullet}$.

However, the lowest degradation of ACT was observed at acidic media (pH = 4.0, and 5.0) which can be attributed to the formation of H-band between the H^+ and O–O group on HSO_5^-. This behavior caused an increase in the positive charge of this molecule and decreased the reaction rate between HSO_5^- and the positive

charge of catalyst. In overall, the photocatalytic activity of as-made catalyst was influenced i) by the PMS activation, ii) the reaction between generated holes (h^+) and hydroxyl ions which occurs at basic media, and iii) the subsequent generation of $HO^\bullet$. Therefore, the 1.0% w/w Ag/$ZnO_{0.04}$@$NiFe_2O_4$/PMS/UVA system works better in the circumneutral pH conditions.

The QY and FoM values for the photocatalytic systems employing $NiFe_2O_4$, $ZnO_{0.04}$@$NiFe_2O_4$, and 1.0% w/w Ag/$ZnO_{0.04}$@$NiFe_2O_4$ nanocomposites were calculated, and the obtained results are shown in Fig. S5 (see Supplementary Text ST5). Based on these results, the highest QY value of 1.39×10^{-3} molecule/photon was seen for 1.0% w/w Ag/$ZnO_{0.04}$@$NiFe_2O_4$ photocatalyst that is 2.05, and 5.63 times higher than $ZnO_{0.04}$@$NiFe_2O_4$, and $NiFe_2O_4$, respectively. In order to evaluate the practical worth of the system, the FoM values were calculated by incorporating of four important performance variables (Fig. S5). The FoM values were calculated to be 0.076, 0.114, and 0.122 in the presence of $NiFe_2O_4$, $ZnO_{0.04}$@$NiFe_2O_4$, and 1.0% w/w Ag/$ZnO_{0.04}$@$NiFe_2O_4$ coupling with UVA/PMS. Effective modification of $NiFe_2O_4$ by using ZnO and Ag NPs in photocatalytic application was highlighted via these parameters.

3.3.2. Effect of water matrix on ACT degradation

The presence of various ions can affect the ACT degradation processes, especially in reactive oxygen species (ROS)-based reactions. In order to evaluate this effect on ACT degradation by 1.0% w/w Ag/$ZnO_{0.04}$@$NiFe_2O_4$/UVA/PMS system, the reaction was carried out in the presence of different ions including chloride (Cl^-), sulfate (SO_4^{2-}), bicarbonate (HCO_3^-), phosphate (PO_4^{3-}), and nitrate (NO_3^-) (the concentration of each ions was 50.0 mg/L), which is high enough to present any antagonistic effects (Rommozzi et al., 2020). Moreover, due to study the effect of mixture of ions on ACT degradation, the reaction was also tested in the tap water. As presented in Fig. 5e, among of different ions that used in this reaction, the highest ACT% removal was obtained in the presence of bicarbonate and chloride ions, followed by nitrate, sulfate and phosphate.

Bicarbonate ions have notable effect on radical-based processes. By addition of bicarbonate ions into the reaction, due to scavenging of $SO_4^{\bullet-}$, and $HO^\bullet$ (eqns. 15 and 16), the reaction efficiency was decreased, and only 42.64% ACT removal efficiency was obtained. The HCO_3^- concentration in natural water is around 0-300 mg/L and can react with both $SO_4^{\bullet-}$, and $HO^\bullet$ at rate constants of 1.6-9.1 × 10^6 M^{-1} s^{-1}, and 8.5-10 × 10^6 M^{-1} s^{-}

[1], respectively (Ji et al., 2015). Due to presence of high concentration of bicarbonate ions (50 mg/L) during the reaction which can affect the generated radicals ($SO_4^{\bullet-}$, and $HO^{\bullet}$), the lowest efficiency was obtained in the presence of this ion. Nevertheless, a little alleviation is achieved since HCO_3^- and/or CO_3^{2-} ions can react with photo-generated species such as holes (h^+) and $HO^{\bullet}$, and produce carbonate radicals ($CO_3^{\bullet-}$) which can react with contaminants (1.9×10^9 M^{-1} s^{-1}) (Wojnarovits et al., 2020). However, $CO_3^{\bullet-}$ is a less selective oxidant than h^+ and $HO^{\bullet}$ in photocatalytic degradation process (eq. 17).

$$HCO_3^- + SO_4^{\bullet-} \longrightarrow HCO_3^{\bullet} + SO_4^{2-} \qquad k_{HCO_3^-/SO_4^{\bullet-}} = 1.6 - 9.1 \times 10^6\ M^{-1}s^{-1} \tag{15}$$

$$HCO_3^- + HO^{\bullet} \longrightarrow CO_3^{\bullet-} + H_2O \qquad k_{HCO_3^-/HO^{\bullet}} = 8.5 - 10 \times 10^6\ M^{-1}s^{-1} \tag{16}$$

$$HCO_3^- + h_{VB}^+ \longrightarrow CO_3^{\bullet-} + H_2O \tag{17}$$

Due to the reaction between chloride ions and the generated sulfate/hydroxyl radicals during the reaction, some oxidative species such as $Cl^{\bullet}$, and $Cl_2^{\bullet-}$ radicals, and $HOCl^{\bullet-}$ can be produced, that can reduce the ACT degradation efficiency. In fact, chloride ions can scavenge $SO_4^{\bullet-}$, and hinder ACT degradation. All mentioned radicals produced in these reactions (eqns. 18-22) have less reactivity compared to $SO_4^{\bullet-}$. Under natural and basic conditions, the generated $HOCl^{\bullet-}$ can decompose back into the Cl^-, and $HO^{\bullet}$ (Rommozzi et al., 2020). Cl^- can react with $HO^{\bullet}$ ten times higher than $SO_4^{\bullet-}$ that affect the reaction efficacy and confirmed the role of these radicals in ACT degradation. In addition, in the presence of Cl^-, the activation rate of PMS by 1.0% w/w Ag/$ZnO_{0.04}$@$NiFe_2O_4$ was decreased, due to reaction between Cl^-, and HSO_5^- resulting in formation HOCl, and Cl_2 (eqns. 23 and 24) (Golshan et al., 2018).

$$Cl^- + SO_4^{\bullet-} \longrightarrow Cl^{\bullet} + SO_4^{2-} \qquad k_{Cl^- + SO_4^{\bullet-}} = 2.8 \times 10^8\ M^{-1}s^{-1} \tag{18}$$

$$Cl^{\bullet} + Cl^- \longrightarrow Cl_2^{\bullet-} \qquad k_{Cl^- + Cl^{\bullet}} = 8.0 \times 10^9\ M^{-1}s^{-1} \tag{19}$$

$$HO^{\bullet} + Cl^- \longrightarrow HOCl^{\bullet-} \qquad k_{Cl^- + HO^{\bullet}} = 3.0 - 4.3 \times 10^9\ M^{-1}s^{-1} \tag{20}$$

$$HO^{\bullet} + Cl^- + O_2 \longrightarrow HOCl + O_2^{\bullet-} \tag{21}$$

$$HOCl^{\bullet-} + H^+ \longrightarrow Cl^{\bullet} + H_2O \tag{22}$$

$$HSO_5^- + Cl^- \longrightarrow SO_4^{2-} + HOCl \tag{23}$$

$$HSO_5^- + 2Cl^- + H^+ \longrightarrow SO_4^{2-} + Cl_2 + H_2O \quad (24)$$

It should be noted that NO_3^- can affect photo-oxidation and photocatalysis processes through the absorption of light (Moradi et al., 2020). In this study, by addition of nitrate ions, the reaction efficiency decreased and the ACT degradation dropped from 100% to 59.65%; this can be attributed to the adsorption and reduction of NO_3^- on the surface of catalyst. Moreover, NO_3^- would be transformed into $NO_3^{\bullet}$, and $NO_2^{\bullet}$ with lower redox potential (2.3, and 1.03 V, respectively) by the trapping of $SO_4^{\bullet-}$, and $HO^{\bullet}$ (eqns. 25 and 26) (Golshan et al., 2018). Also, NO_3^- can react with photo-generated e^- with rates ranging around 8.6-11 × 10^9 M^{-1} s^{-1} resulting in the formation of $NO_2^{\bullet}$, that can affect the removal efficiency in the photocatalytic reaction (eq. 27) (De la Mora et al., 2011). It should also be considered that under UVA irradiation, NO_3^- can act as source of $NO_2^{\bullet}$ and $HO^{\bullet}$ (eq. 28) (Rommozzi et al., 2020, Xu et al., 2020c). However, the competition between the scavenging effect by NO_3^- and its action as source of $HO^{\bullet}$ had an unfavorable equilibrium, hence the reaction efficiency was decreased in the presence of NO_3^- ions. As such, the presence of inorganic ions in photocatalytic reactions can inhibit the reaction efficiency not only by scavenging of free radicals, but also decreasing the influence of light irradiation, and also increasing the competition for active sites with contaminants.

$$NO_3^- + SO_4^{\bullet-} \longrightarrow NO_3^{\bullet} + SO_4^{2-} \qquad k = 3.6 \times 10^5\ M^{-1}s^{-1} \quad (25)$$

$$NO_3^- + HO^{\bullet} \longrightarrow NO_3^{\bullet} + HO^- \qquad k = 8.8 \times 10^7\ M^{-1}s^{-1} \quad (26)$$

$$NO_3^{\bullet} + H_2O + e^- \longrightarrow NO_2^{\bullet} + 2HO^- \qquad k = 8.6 - 11 \times 10^9\ M^{-1}s^{-1} \quad (27)$$

$$NO_3^- + H_2O + h\nu \longrightarrow NO_2^{\bullet} + HO^- + HO^{\bullet} \quad (28)$$

According to the obtained results, the presence of sulfate ions has negative effect on reaction efficiency. This ion can normally scavenge the generated $HO^{\bullet}$, and h^+ which can influence on rate of reaction (eqns. 29, and 30). It should be considered that reaction 29 can occurred significantly only at pH < 3.0, in which $SO_4^{\bullet-}$ generated (Rommozzi et al., 2020).

$$SO_4^{2-} + HO^{\bullet} \longrightarrow SO_4^{\bullet-} + OH^- \qquad pH < 3.0 \quad (29)$$

$$SO_4^{2-} + h_{VB}^+ \longrightarrow SO_4^{\bullet-} \quad (30)$$

Phosphate ions are an important sink for $SO_4^{\bullet-}$ and $HO^{\bullet}$. The concentration of phosphate has vital role in degradation efficiency. According to obtained results, in the presence of phosphate ions (50.0 mg/L) the ACT removal was decreased to 78.60%. The phosphate can scavenge $HO^{\bullet}$ and the photo-generated h^+ while

producing other weaker radicals. Among the various ions assessed in this study, the lowest effect on ACT degradation was observed in the presence of phosphate ions. The reaction rate constant between phosphate ions and $SO_4^{\bullet-}$ (1.2-16 × 10^6 M^{-1} s^{-1}) is 100 times higher than $HO^{\bullet}$ (2.0-15 × 10^4 M^{-1} s^{-1}). So, the phosphate ion is an effective quencher for $SO_4^{\bullet-}$ when compared with $HO^{\bullet}$ (Sheng et al., 2018). So we can postulate that in our system $HO^{\bullet}$ is most likely the dominant reactive species, since it demonstrate the lowest inhibition in the presence of phosphate ions. In any case, the results of the ion-inhibition study can indicate the role of $SO_4^{\bullet-}$, and $HO^{\bullet}$ during the reaction; the reactivity of $HO^{\bullet}$ with the tested ions is decreasing as following Cl^- > HCO_3^- > PO_4^{3-}, while this trend decreasing for $SO_4^{\bullet-}$ as follows: Cl^- > HCO_3^- > PO_4^{3-} > NO_3^-.

3.4. Stability and recyclability of the synthesized nano-photo-catalyst

From the mechanical and economical point of view, the recyclability of catalyst is an important parameter for practical applications. In order to study these properties, the catalyst was used in consecutive reaction cycles under the optimum reaction conditions. Based on the results reported in Fig. S6a, ACT removal in the 1st, 2nd, 3rd, and 4th runs were 100%, 100%, 100%, and 95%, respectively. These results indicated that the 1.0% w/w Ag/$ZnO_{0.04}$@$NiFe_2O_4$ catalyst has high reusability and could be considered as a stable photocatalyst in PMS activation. This excellent reusability was confirmed by using the ICP-AES analysis (Fig. S6b), in which very low amount of Ag, Fe, Zn, and Ni was leached from the nanocomposite into the reaction media (see Supplementary Text ST6). In addition, the high structural stability of the reused catalyst was verified by XRD (Fig. S6c), and XPS analysis (for more details see Supplementary Text ST7). The XRD patterns of pristine and recovered catalysts (after 4 runs) were identical. All the characteristic peaks related to $NiFe_2O_4$, ZnO, and Ag NPs were observed and confirmed that the structure was preserved after four consecutive photocatalytic runs. Moreover, the XPS analysis showed that there is practically no differences in the binding energies of Ni 2p, Fe 2p, O 1s, Zn 2p and Ag 3d orbitals between pristine and reused catalysts. In this sense, the oxidation states of Ni cation (+2), Fe cation (+3), Zn cation (+2) and Ag (0) in the reused catalyst were not affected by the degradation process (Fig. S7).

3.5. Mechanistic considerations on the photocatalytic PMS activation and the pathways leading to ACT degradation

3.5.1. Integrated mechanism proposition leading to ACT degradation

In order to investigate the main photo-produced reactive intermediates formed during the photocatalytic removal of ACT coupling with UVA/PMS, scavenger experiments were deployed. Different scavengers including oxalate (OX), *tert*-butyl alcohol (TBA), ethanol (EtOH), and *p*-benzoquinone (BQ) were applied in the ACT degradation under the selected conditions. As illustrated in Fig. 5f, in the presence of BQ ($O_2^{\bullet-}$ scavenger), OX (h^+ scavenger), TBA ($HO^\bullet$ scavenger), and EtOH ($SO_4^{\bullet-}$ and $HO^\bullet$ scavenger) ACT removal efficiency was decreased to 73.0%, 56.2%, 53.0%, and 37.3%, respectively. Based on these results, $SO_4^{\bullet-}$ $HO^\bullet$, h^+, and $O_2^{\bullet-}$ were involved in ACT degradation by the 1.0% w/w Ag/$ZnO_{0.04}$@$NiFe_2O_4$ catalyst, assisted by UVA and PMS.

The high reduction of ACT degradation in the presence of EtOH confirmed the role of both $HO^\bullet$ and $SO_4^{\bullet-}$ in this reaction. The rate constant of reaction between TBA and EtOH with $HO^\bullet$ is (3.6-7.6) × 10^8 M^{-1} s^{-1} and (1.2-2.8) × 10^9 M^{-1} s^{-1}, while these values for $SO_4^{\bullet-}$ are (4.0-9.1) × 10^5 M^{-1} s^{-1}, and (1.6-7.7) × 10^7 M^{-1} s^{-1}, respectively (Kohantorabi et al., 2021b). Based on these values, TBA can react with $HO^\bullet$ 1000 times faster than $SO_4^{\bullet-}$, while EtOH has a similar effect on the reaction between $HO^\bullet$ and $SO_4^{\bullet-}$. As such, the combination of these tests can isolate the role of $HO^\bullet$ in this reaction.

The first order rate constant values for the catalyst/PMS/UVA process, and catalyst/PMS/UVA + TBA as hydroxyl radical scavenger were calculated to be 0.368 min^{-1} and 0.0541 min^{-1}, respectively (Fig. S8). According to these results in the presence of TBA, the reaction rate decreased and the value is about 6.8-fold lower than of the respective one in the catalyst/PMS/UVA process. The $SO_4^{\bullet-}$ can react with organic compounds through electron transfer process, while the $HO^\bullet$ do it by using two reactions such as electron transfer, and hydrogen-atom abstraction (Rastogi et al., 2009). So, the degradation of ACT by the as-made catalyst coupled with UVA+PMS has very high efficiency that is attributed to the different $SO_4^{\bullet-}$ and $HO^\bullet$ reaction pathways, and high stability of PMS during the reaction.

In order to assess the possibility of this pathway, the level of valence (VB) and conduction (CB) bands of our semiconductors were calculated by the following equations (eqns. 31 and 32):

$$E_{VB} = \chi - E^e + 0.5\, E_g \quad (31)$$

$$E_{CB} = E_{VB} - E_g \quad (32)$$

Where, E_g, E^e, and χ are the band gap energy, free energy of electron in hydrogen scale (4.5 eV), and the absolute electronegativity of the semiconductors, respectively (Rastogi et al., 2009). According to these equations, the VB and CB energies of $NiFe_2O_4$ are +1.09 eV, and -0.79 eV, and those for ZnO are +3.0 eV, and -0.12 eV, respectively. Under UVA light irradiation, the semiconductors can absorb the photons and generate the electron/hole pairs (eq. 33). The CB potential of $NiFe_2O_4$ is higher than CB of ZnO and is more negative than the redox potential of $O_2/O_2^{\bullet-}$ (-0.33 eV). Based on this property, the oxygen molecules can react with photo-generated electron in as-made photocatalyst, hence $O_2^{\bullet-}$ can be produced (eq. 34). Additionally, among the rest of the reactive species generated in our process, $O_2^{\bullet-}$ had a relatively minor role in ACT photocatalytic degradation; only a 27% decrease was observed in the presence of BQ as $O_2^{\bullet-}$ scavenger during the reaction ($k_{O_2^{\bullet-}}$ = 0.9-1.0 × 10^9 M^{-1} s^{-1}). Nevertheless, behind this small contribution, there are two indirect pathways associated with $O_2^{\bullet-}$, which merit further discussion.

i) $O_2^{\bullet-}$ could also be implicated in the generation of $HO^{\bullet}$. $HO^{\bullet}$ can be generated through two reactions: i) direct oxidization of HO^- with photo-generated holes (will be proven afterwards, see below), and ii) reaction of $O_2^{\bullet-}$ with H^+, and e^-/h^+ (eqns. 35 and 36) (Abdel Messih et al., 2019). Both reactions can enhance the photocatalytic activity of the as-prepared catalyst in ACT degradation. Moreover, the photo-generated e^- in the CB of ZnO can be transferred to the Fermi level of Ag NPs that can suppress the e^-/h^+ recombination (Abdel Messih et al., 2019). Ag NPs in the as-made photocatalyst act as electron conduits that enhance the generation of $O_2^{\bullet-}$, and subsequently $HO^{\bullet}$.

ii) The generated $O_2^{\bullet-}$ can be decompose the adsorbed PMS and H_2O molecules on the surface of catalyst, to produce $SO_4^{\bullet-}$ and $HO^{\bullet}$, respectively (eqns. 37 and 38) (Golshan et al., 2018).

$$Photocatalyst + hv \longrightarrow e_{CB}^- + h_{VB}^+ \quad (33)$$

$$e_{CB}^- + O_2 \longrightarrow O_2^{\bullet-} \quad (34)$$

$$O_2^{\bullet-} \xrightarrow{H^+} HOO^{\bullet} \longrightarrow HO^{\bullet} \quad (35)$$

$$O_2^{\bullet -} \xrightarrow{e^-/h^+} H_2O_2 \xrightarrow{e^-} HO^{\bullet} \quad (36)$$

$$O_2^{\bullet -} + HSO_5^- \longrightarrow SO_4^{\bullet -} + HO_2^- \quad (37)$$

$$O_2^{\bullet -} + H_2O \longrightarrow HO^{\bullet} + HO^- \quad (38)$$

$$h_{VB}^+ + H_2O \longrightarrow HO^{\bullet} + H^+ \quad (39)$$

$$h_{VB}^+ + HO^- \longrightarrow HO^{\bullet} \quad (40)$$

Finally, the VB edge potential of ZnO shell (+3.0 eV) is more positive than the VB edge of $NiFe_2O_4$ hence photo-generated holes can be transferred into the VB edge of $NiFe_2O_4$. The photo-generated h^+ not only can directly react with ACT molecules and degrade them but also by the reaction between h^+ and HO^-, $HO^{\bullet}$ can be obtained, which enhance the photocatalytic performance (eqns. 39 and 40).

Due to the presence of PMS as oxidant, the mechanism of reaction can be explained in two parts. First part is related to the photocatalytic property of catalyst which was discussed above, and the second part corresponding to the PMS activation by the 1.0% w/w $Ag/ZnO_{0.04}@NiFe_2O_4$ nanocomposite. By the oxidation cycles of Fe^{3+}/Fe^{2+}, and Ni^{2+}/Ni^{3+} in the sample, PMS can generate $SO_4^{\bullet -}$ and $HO^{\bullet}$ (Ghanbari et al., 2019; Xu et al., 2020c). Also, PMS can act as electron acceptor in the photocatalytic processes. By this reaction PMS can be activated by the generated e^-/h^+ pairs and both of $SO_4^{\bullet -}$ and $HO^{\bullet}$ are produced (eq. 41). As a result, ACT was degraded and mineralized by generated ROS in the bulk solution (eq. 42).

$$HSO_5^- + e_{CB}^- \longrightarrow HO^- + SO_4^{\bullet -} \; or \; HO^{\bullet} + SO_4^{2-} \quad (41)$$

$$HO^{\bullet}/SO_4^{\bullet -}/h_{VB}^+/O_2^{\bullet -} + pollutant \longrightarrow By-products \quad (42)$$

To summarize, based on the scavenger experiments and the above described pathways, Fig. 6 depicts the mechanism of ACT degradation in the PMS/UVA photocatalytic process with the 1.0% w/w $Ag/ZnO_{0.04}@NiFe_2O_4$ nanorod.

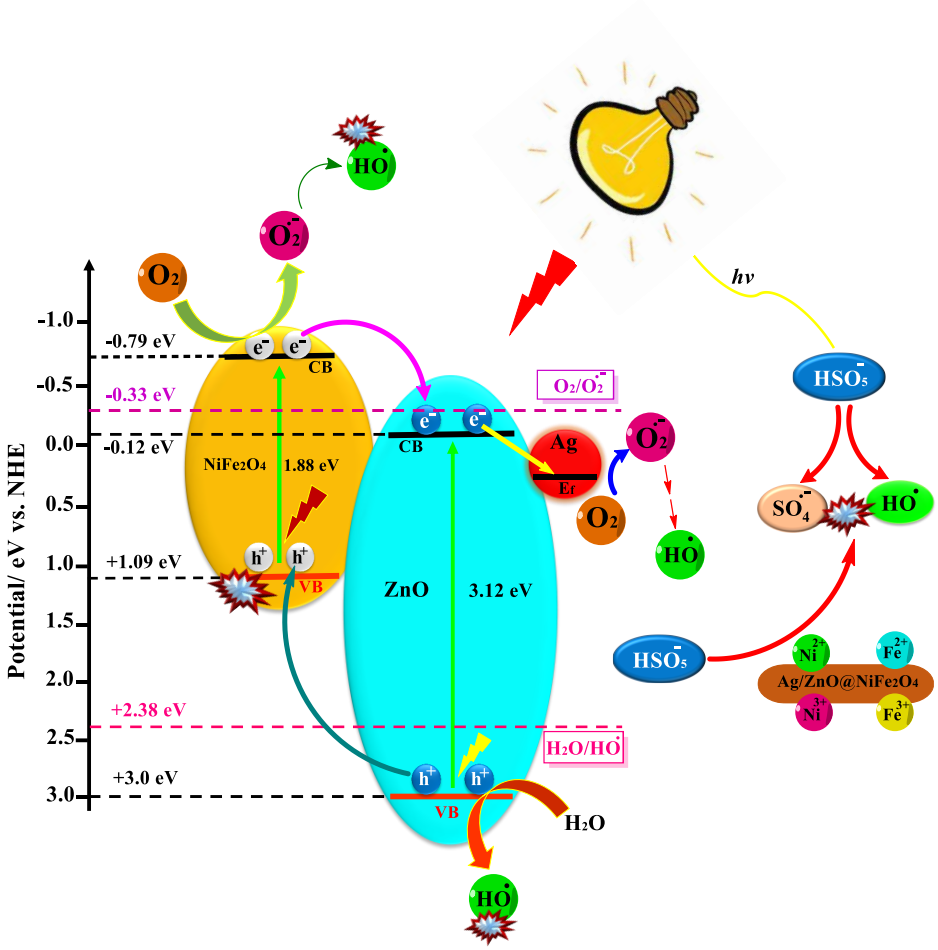

Figure 6. Mechanism of ACT degradation in 1.0% w/w Ag/$ZnO_{0.04}$@$NiFe_2O_4$/UVA/PMS process.

3.5.2. Investigation of the ACT degradation pathway by intermediates identification via LC-MS analysis

In order to investigate the by-products and intermediates generation during the photocatalytic degradation of ACT over the 1.0% w/w Ag/$ZnO_{0.04}$@$NiFe_2O_4$ nanocomposite coupled with PMS/UVA under the optimum conditions, LC-MS analysis was applied. According to obtained results, eleven transformation products (TPs) were detected based on their mass-to-charge (*m/z*) ratio; the degradation reaction pathway in the catalyst/PMS/UVA process was proposed and reported in Fig. 7. In AOPs, the degradation pathway consists of competitive reactions including hydroxylation of aromatic ring, carboxylation, dehalogenation, C-N bond cleavage and ring opening that cause to formation of aliphatic compounds such as acetic acid, etc. (Moradi et al., 2020). Based on the mechanism evaluation of ACT in the presence process, two reactive species including $HO^{\bullet}$, and $SO_4^{\bullet-}$ were involved in ACT degradation reaction. According to the literature in AOPs, hydroxylation is a dominant degradation pathway especially in UV-based AOPs (Alharbi et al., 2017). By the hydroxylation,

hydroxyl group is connected to the aromatic ring and produced the TP1, which leads to formation of 1, 4-dihydroxybenzene (TP4), and glycolic acid (TP5) as *a*–hydrogen acid. Following, TP3, and TP4 can act as precursors for the generation of 1, 4-benzoquinone (TP8). Due to hydroxylation of TPs by the generated radicals and oxidation of intermediates that lead to breakdown of the aromatic structure and amide bonds, 3-hydroxypropanoic acid (TP10) as linear product was obtained which finally was converted to CO_2 and H_2O. It should be noted that the *m/z* values for two products (TP6, and TP10) were the same, indicating both their simultaneous generation during the degradation of ACT in the present system. The appearance of nitrate (TP7, *m/z* = 62) as an inorganic intermediate in LC-Ms spectra of this system, indicated the high oxidation efficiency of nitrogen-containing bonds in ACT structure, as well as the degradation of related intermediates.

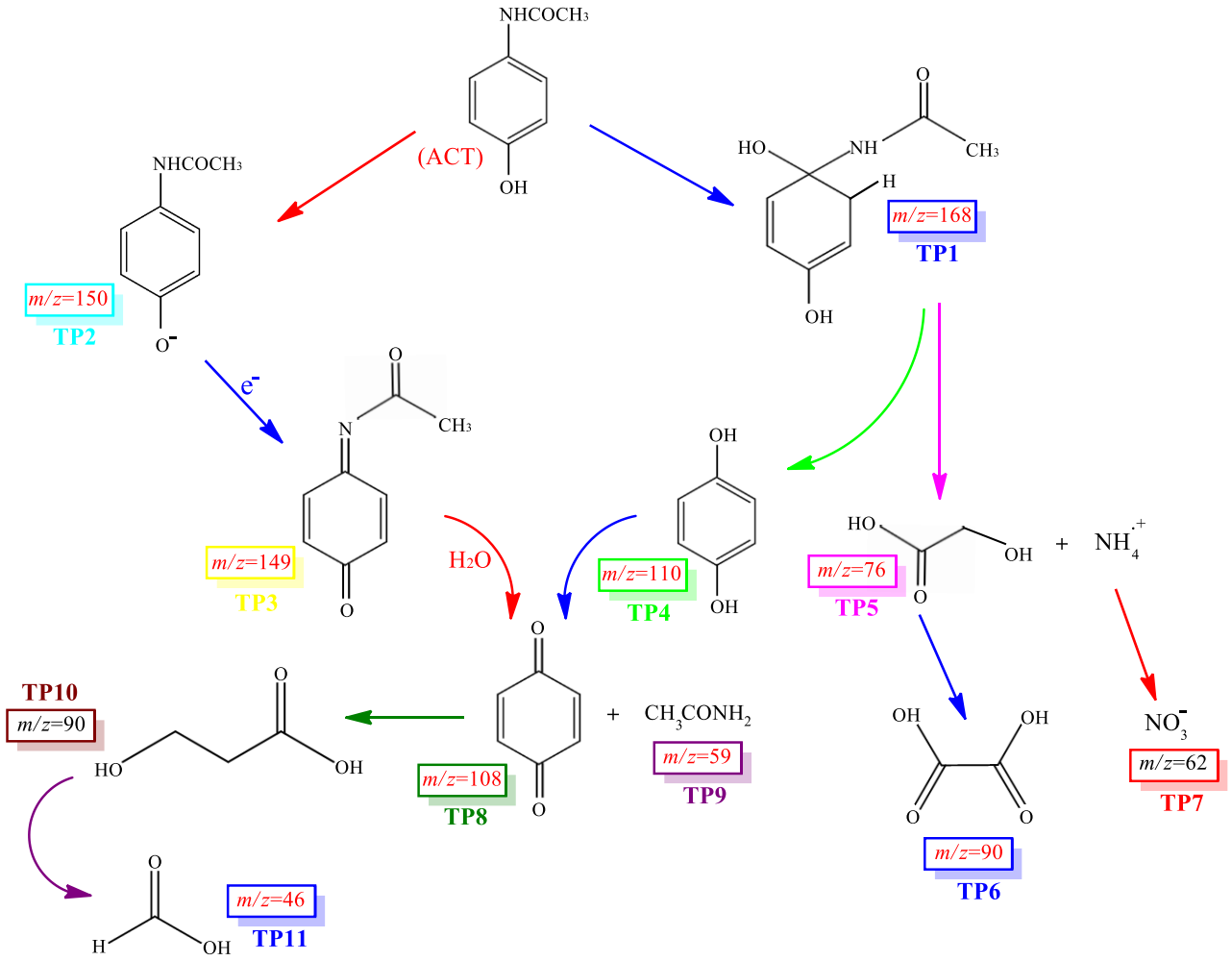

Figure 7. Proposed pathway of ACT degradation over the 1.0% w/w $Ag/ZnO_{0.04}@NiFe_2O_4$/UVA/PMS process (Reaction conditions: [ACT] = 12.0 mg/L, [PMS] = 0.2 mM, [catalyst] = 0.1 g/L, Solution pH = 7.0, and reaction time = 60 min).

4. Conclusions

In the present study, a mesoporous ZnO@$NiFe_2O_4$ nanorod derived from a Fe_2Ni-MIL-88 MOF was successfully synthesized by a facile synthesis method. The obtained 1.0% w/w Ag/$ZnO_{0.04}$@$NiFe_2O_4$ nanocomposite exhibited the high catalytic performance in activation of PMS for ACT degradation under UVA-LED. The ACT removal efficiency in $NiFe_2O_4$/PMS, and 1.0% w/w Ag/$ZnO_{0.04}$@$NiFe_2O_4$/PMS under UVA irradiation was obtained to be 62.2%, and 100% during 15 min, while the k_{app} values for these reactions were calculated to be 0.065 min^{-1}, and 0.368 min^{-1}, respectively. By introducing the Ag NPs on the surface of catalyst, the recombination rate of electron/hole (e^-/h^+) pairs in photocatalytic reaction was decreased, increasing the generation of $O_2^{\bullet-}$ and in turn $HO^\bullet$ as active species. The order of importance generated species in the degradation of ACT was found as follows: $HO^\bullet > SO_4^{\bullet-} > h^+ > O_2^{\bullet-}$. Hence, the as-made catalyst derived from Fe_2Ni-MIL-88 showed a high activity for PMS activation under UVA light for the degradation of ACT from water. In conclusion, this study introduces new insights in the preparation of catalyst derived from MOFs, with potential environmental applications in pollutants degradation.

5. Acknowledgments

This work was technically and financially supported by the Tarbiat Modares University, Iran, under the Research Group grant No. IG-39801. Stefanos Giannakis would like to acknowledge the Spanish Ministry of Science, Innovation and Universities (MICIU) for the Ramón y Cajal Fellowship (RYC2018-024033-I).

6. References

Zhang, Y. T., Liu, C., Xu, B. B., Qi, F., Chu, W., 2016. Degradation of benzotriazole by a novel Fenton-like reaction with mesoporous Cu/MnO_2: combination of adsorption and catalysis oxidation. *Appl. Catal. B Environ*. 199, 447-457.

Giannakis, S., Samoili, S., Rodriguez-Chueca, J., 2021a. A meta-analysis of the scientific literature on (photo) Fenton and persulfate advanced oxidation processes: Where do we stand and where are we heading to? *Curr. Opin. Green Sustain*. 29, 100456.

Guan, C., Jiang, J., Luo, C., Pang, S., Yang, Y., Wang, Z., ma, J., Yu, J., Zhao, X., 2018. Oxidation of bromophenols by carbon nanotube activated peroxymonosulfate (PMS) and formation of brominated products: Comparison to peroxydisulfate (PDS). *Chem. Eng. J*. 337, 40-50.

Hu, P., Long, M., 2016. Cobalt-catalyzed sulfate radical-based advanced oxidation: A review on heterogeneous catalysts and applications. *Appl. Catal. B Environ*. 181, 103-117.

Kohantorabi, M., Moussavi, G., Giannakis, S., 2021a. A review of the innovations in metal- and carbon-based catalysts explored for heterogeneous peroxymonosulfate (PMS) activation, with focus on radical vs. non-radical degradation pathways of organic contaminants. *Chem. Eng. J*. 411, 127957.

Wang, C., Kim, J., Malgras, V., Na, J., Lin, J., You, J., Zhang, M., Li, J., Yamauchi, Y., 2019. Metal–Organic Frameworks and Their Derived Materials: Emerging Catalysts for a Sulfate Radicals-Based Advanced Oxidation Process in Water Purification. *Small*. 15 (16), 1900744.

Wang, Z.P., Chen, Y.Q., Xie, P.C., Shang, R., Ma, J., 2016. Removal of Microcystisaeruginosa by UV-activated persulfate: performance and characteristics. *Chem. Eng. J*. 300, 245-253.

Giannakis, S., Lin, K. Y. A., Ghanbari, F., 2021b. A review of the recent advances on the treatment of industrial wastewaters by Sulfate Radical-based Advanced Oxidation Processes (SR-AOPs). *Chem. Eng. J.* 406, 127083.

Rodriguez-Chueca, J., Giannakis, S., Marjanovic, M., Kohantorabi, M., Gholami, M. R., Grandjean, D., de Alencastro, L. F., Pulgarin, C., 2019. Solar-assisted bacterial disinfection and removal of contaminants of emerging concern by Fe^{2+}-activated HSO_5^- *vs*. $S_2O_8^{2-}$ in drinking water. *Appl. Catal B: Environ*. 248, 62-72.

Li, Z., Liu, D., Zhao, Y., Li, S., Wei, X., Meng, F., Huang, W., Lei, Z., 2019. Singlet oxygen dominated peroxymonosulfate activation by CuO-CeO_2 for organic pollutants degradation: Performance and mechanism. *Chemosphere*. 233, 549-558.

Kohantorabi, M., Gholami, M. R., 2017. M_xNi_{100-x} (M = Ag, and Co) nanoparticles supported on CeO_2 nanorods derived from Ce–metal organic frameworks as an effective catalyst for reduction of organic pollutants: Langmuir–Hinshelwood kinetics and mechanism. *New J. Chem.* 41, 10948-10958.

Xu, Y., Shi, X., Hua, R., Zhang, R., Yao, Y., Zhao, B., Liu, T., Zheng, J., Lu, G., 2020a. Remarkably catalytic activity in reduction of 4-nitrophenol and methylene blue by Fe_3O_4@COF supported noble metal nanoparticles. *Appl. Catal. B: Environ*. 260, 118142.

Khan, A., Liao, Z., Liu, Y., Jawad, A., Ifthikar, J., Chen, Z., 2017. Synergistic degradation of phenols using peroxymonosulfate activated by CuO-Co_3O_4@MnO_2 nanocatalyst. *J. Hazard. Mater*. 329, 262-271.

Huang, Y. F., Sun, X. Y., Huo, S. H., Li, Y., Zhong, C., 2019. Core-shell dual-MOF heterostructures derived magnetic $CoFe_2O_4$/CuO (sub) microcages with superior catalytic performance. *Appl. Surf. Sci*. 466, 637-646.

Liu, J., Zhao, Z., Shao, P., Cui, F., 2015. Activation of peroxymonosulfate with magnetic Fe_3O_4–MnO_2 core–shell nanocomposites for 4-chlorophenol degradation. *Chem. Eng. J*. 267, 854-861.

Zhu, K., Wang, J., Wang, Y., Jin, C., Ganeshraja, A. S., 2016. Visible-Light-Induced Photocatalysis and Peroxymonosulfate Activation over $ZnFe_2O_4$ Fine Nanoparticles for Degradation of Orange II. *Catal. Sci. Technol*. 6, 2296-2304.

Ding, M., Chen, W., Xu, H., Shen, Z., Lin, T., Hu, K., Lu, C. H., Xie, Z., 2020. Novel α-Fe_2O_3/MXene nanocomposite as heterogeneous activator of peroxymonosulfate for the degradation of salicylic acid. *J. Hazard. Mater*. 382, 121069.

Shen, C. H., Wen, X. J., Fei, Z. H., Liu, Z. T., Mu, Q. M., 2020. Visible-light-driven activation of peroxymonosulfate for accelerating ciprofloxacin degradation using CeO_2@Co_3O_4 p-n heterojunction photocatalysts. *Chem. Eng. J*. 391, 123612.

Reza, N., Reza, W., Gul, H., Azam, M., Lee, J., Vikrant, K., Kim, K. H., 2020. Solar-light-active silver phosphate/titanium dioxide/silicaheterostructures for photocatalytic removal of organic dye. *J. Clean. Product*. 254, 120031.

Salari, H., 2019. Kinetics and mechanism of enhanced photocatalytic activity under visible light irradiation using Cr_2O_3/Fe_2O_3 nanostructure derived from bimetallic metal organic framework. *J. Environ. Chem. Eng*. 7 (3), 103092.

Li, S., Tan, J., Jiang, Z., Wang, J., Li, Z., 2020. MOF-derived bimetallic Fe-Ni-P nanotubes with tunable compositions for dye-sensitized photocatalytic H_2 and O_2 production. *Chem. Eng. J*. 384, 123354.

Sudhaik, A., Raizada, P., Shandilya, P., 2018. Magnetically recoverable graphitic carbon nitride and $NiFe_2O_4$ based magnetic photocatalyst for degradation of oxytetracycline antibiotic in simulated wastewater under solar light. *J. Ind. Eng. Chem*. 6 (4), 3874-3883.

Sakhare, P. A., Pawar, S. S., Bhat, T. S., Yadav, S. D., Patil, G. R., Patil, P. S., Sheikh, A. D., 2020. Magnetically Recoverable $BiVO_4$/$NiFe_2O_4$ Nanocomposite Photocatalyst For Efficient Detoxification of Polluted Water Under Collected Sunlight. *Mater. Res. Bull*., 129, 110908.

Khavar, A. H. C., Moussavi, G., Mahjoub, A., Yaghmaeian, K., Srivastara, V., Sillanpaa, M., Satari, M., 2019. Novel magnetic Fe_3O_4@rGO@ZnO onion-like microspheres decorated with Ag nanoparticles for the efficient photocatalytic oxidation of metformin: toxicity evaluation and insights into the mechanisms. *Catal. Sci. Technol*. 9, 5819-5837.

Vikrant, K., Park, C. M., Kim, K. H., Kumar, S., Jeon, E. C., 2019. Recent advancement in photocatalyst-based platforms for the destruction of gaseous benzene: Performance evaluation of different modes of photocatalytic operations and against adsorption technique. *J. Photochem. Photobio C*. 41, 100316.

Wang, Y., Hu, K., Yang, Z., Ye, C., Li, X., Yan, K., 2021. Synthesis of Porous ZnO Nanoparticles Efficient for Photocatalytic Degradation of Biomass-Derived Bisphenol A under Simulated Sunlight Irradiation. *Front. Bioeng. Biotechnol*. 8, 616780.

Shi, J., Li, Sh., Wang, F., Li, Y., Gao, L., Zhanga, X., Lu, J., 2018. In situ topotactic fabrication of direct Z-scheme 2D/2D ZnO/$Zn_xCd_{1-x}S$ single crystal nanosheet heterojunction for efficient photocatalytic water splitting. *Catal. Sci. Technol*. 8, 6458-6467.

Zhou, Y., Chen, G., Yu, Y., Zhao, L., Yu, Q., He, Q., 2016. Effect of La-doping on charge separation behavior of ZnO: GaN for its enhanced photoctalytic performance. *Catal. Sci. Technol*. 6, 1033-1041.

Lee, T., Chao, B. K., Kuo, Y. L., Hsueh, C. H., 2017. Improvement of photocatalytic activities of Ag/P25 hybrid system by controlled morphology of Ag nanoprisms. *Mater. Chem. Phys*. 192, 78-85.

Chen, J. J., Wu, J. C. S., Wu, P. C., Tsai, D. P., 2012. Improved photocatalytic activity of shell-isolated plasmonic photocatalyst Au@SiO_2/TiO_2 by promoted LSPR. *J. Phys. Chem. C*. 116, 26535-26542.

Luo, N., Zhang, B., Zhang, D., Xu, J., 2020. Enhanced CO sensing properties of Pd modified ZnO porous nanosheets. *Chines. Chem. Lett*., 31 (8), 2033-2036.

Uen, K., Misawa, H., 2013. Surface plasmon-enhanced photochemical reactions. *J. Photochem. Photobiol. C*. 15, 31-52.

Xiao, X., Wei, J., Yang, Y., Xiong, R., Pan, C., Shi, J., 2016. Photoreactivity and mechanism of gC_3N_4 and Ag Co-Modified Bi_2WO_6 microsphere under visible light irradiation. *ACS Sustainable Chem. Eng*. 4, 3017-3023.

Fu, M., Jiao, Q., Zhao, Y., 2013. Preparation of $NiFe_2O_4$ nanorod–graphene composites via an ionic liquid assisted one-step hydrothermal approach and their microwave absorbing properties. *J. Mater. Chem. A.* 1(18), 5577-5586.

Jin, C., Lu, F., Cao, X., Yang, Z., Yang, R., 2013. Facile synthesis and excellent electrochemical properties of $NiCo_2O_4$ spinel nanowire arrays as a bifunctional catalyst for the oxygen reduction and evolution reaction. *J. Mater. Chem. A*. 1(39), 12170-12177.

Moulder, J. F., Stickle, W. F., Sobol, P. F., Kenneth, B. D., 1992. Handbook of X-ray Photoelectron Spectroscopy, 1st ed.; Perkin-Elmer. *Corporation: Eden Prairie*. 44, 80-85.

Xu, X., Li, Y., Zhang, G., Yang, F., He, P., 2019. NiO-$NiFe_2O_4$-rGO Magnetic Nanomaterials for Activated Peroxymonosulfate Degradation of Rhodamine B. *Water*. 11, 384.

Zhou, T., Zhang, R., Wang, Y., Zhang, T., 2019. MOF–Derived 1 D α–Fe_2O_3/$NiFe_2O_4$ heterojunction as efficient sensing materials of acetone vapors. *Sens. Actuators B Chem.* 281, 885-892.

Ortiz-Quiñonez, J. L., Pal, U., Villanueva, M. S., 2018. Structural, Magnetic, and Catalytic Evaluation of Spinel Co, Ni, and Co–Ni Ferrite Nanoparticles Fabricated by Low-Temperature Solution Combustion Process. *ACS Omega*. 3(11), 14986-15001.

Al-Gaashani, R., Radiman, S., Daud, A. R., Tabet, N., Al-Douri, Y., 2013. XPS and optical studies of different morphologies of ZnO nanostructures prepared by microwave methods. *Ceram. Int*. 39(3), 2283-2292.

Van Khai, T., Van Thu, L., Huu, N. T., Lam, T. D., 2016. Vertically Well-Aligned ZnO Nanowire Arrays Directly Synthesized from Zn Vapor Deposition Without Catalyst. *J. Electron. Mater*. 45(5), 2601-2607.

Zou, X. H., Zhao, S. W., Zhang, J. G., Sun, H. L., Pan, Q. J., Guo, Y. R., 2019. Preparation of ternary ZnO/Ag/cellulose and its enhanced photocatalytic degradation property on phenol and benzene in VOCs. *Open Chem. J*. 17(1), 779.

Potlog, T., Duca, D., Dobromir, M., 2015. Temperature-dependent growth and XPS of Ag-doped ZnTe thin films deposited by close space sublimation method. *Appl. Surf. Sci*. 352, 33-37.

Low, J., Yu, J., Li, Q., Cheng, B., 2014. Enhanced visible-light photocatalytic activity of plasmonic Ag and graphene co-modified Bi_2WO_6 nanosheets. *Phys. Chem. Chem. Phys*. 16, 1111-1120.

Salari, H., Kohantorabi, M., 2020. Facile template-free synthesis of new α-MnO_2 nanorod/silver iodide p–n junction nanocomposites with high photocatalytic performance. *New J. Chem*., 44, 7401-7411.

Kohantorabi, M., Giannakis, S., Moussavi, G., Bensimon, M., Gholami, M. R., Pulgarin, C., 2021b. An innovative, highly stable Ag/ZIF-67@GO nanocomposite with exceptional peroxymonosulfate (PMS) activation efficacy, for the destruction of chemical and microbiological contaminants under visible light. 413, 125308.

Pan, X., Xu, Y. J., 2013. Defect-mediated growth of noble-metal (Ag, Pt, and Pd) nanoparticles on TiO_2 with oxygen vacancies for photocatalytic redox reactions under visible light. *J. Phys. Chem. C Nanomater. Interfaces*. 117, 17996-18005.

Ghanbari, F., Ahmadi, M., Gohari, F., 2019. Heterogeneous activation of peroxymonosulfate via nanocomposite CeO_2-Fe_3O_4 for organic pollutants removal: the effect of UV and US irradiation and application for real wastewater. *Sep. Purif. Technol*. 228, 115732.

Ozores-Diez, P., Giannakis, S., Rodriguez-Chueca, J., Wang, D., Quilty, B., Devery, R., McGuigan, K., Pulgarin, C., 2020. Enhancing solar disinfection (SODIS) with the photo-Fenton or the

Fe^{2+}/peroxymonosulfate-activation process in large-scale plastic bottles leads to toxicologically safe drinking water. *Water. Res*., 186, 116387.

Guan, Y. H., Ma, J., Li, X. C., Fang, J. Y., Chen, L. W., 2011. Influence of pH on the Formation of Sulfate and Hydroxyl Radicals in the UV/Peroxymonosulfate System. *Environ. Sci. Technol*. 45 (21), 9308-9314.

Xu, M., Zhou, H., Wu, Z., Li, N., Xiong, Z., Yao, G., Lai, B., 2020b. Efficient degradation of sulfamethoxazole by $NiCo_2O_4$ modified expanded graphite activated peroxymonosulfate: Characterization, mechanism and degradation intermediates. *J. Hazard. Mater*. 399, 123103.

Shukla, P., Fatimah, I., Wang, S., Ang, H. M., Tade, M. O., 2010. Photocatalytic generation of sulphate and hydroxyl radicals using zinc oxide under low-power UV to oxidise phenolic contaminants in wastewater. *Catal. Today*. 157, 410-414.

Tan, C., Gao, N., Deng, Y., Deng, J., Zhou, S., Lia, J., Xin, X., 2014. Radical induced degradation of acetaminophen with Fe_3O_4 magnetic nanoparticles as heterogeneous activator of peroxymonosulfate. *J. Hazard. Mater*. 276, 452-460.

Tan, C., Gao, N., Fu, D., Deng, J., Deng, L., 2017. Efficient degradation of paracetamol with nanoscaled magnetic $CoFe_2O_4$ and $MnFe_2O_4$ as a heterogeneous catalyst of peroxymonosulfate. *Sep. Purif. Technol*. 175, 47-57.

Noorisepehr, M., Ghadirinejad, K., Kakavandi, B., Esfahani, A. R., Asadi, A., 2019. Photo-assisted catalytic degradation of acetaminophen using peroxymonosulfate decomposed by magnetic carbon heterojunction catalyst. *Chemosphere*. 232, 140-151.

Fan, J., Qian, H., Jiang, S., 2019. Mn-doped g-C_3N_4 composite to activate peroxymonosulfate for acetaminophen degradation: The role of superoxide anion and singlet oxygen. *Chem. Eng. J*. 359, 723-732.

Zhu, J., Zhu, Z., Zhang, H., Lu, H., Qiu, Y., 2019. Calcined CoAl-layered double hydroxide as a heterogeneous catalyst for the degradation of acetaminophen and rhodamine B: activity, stability, and mechanism. *Environ. Sci. Pollut. Res*. 26, 33329-33340.

Fanaei, F., Moussavi, G., Srivastava, V., Sillanpaa, M., 2019. The enhanced catalytic potential of sulfur-doped MgO (S-MgO) nanoparticles in activation of peroxysulfates for advanced oxidation of acetaminophen. *Chem. Eng. J*. 371, 404-413.

Rommozzi, E., Giannakis, S., Giovannetti, R., Vione, D., Pulgarin, C., 2020. Detrimental vs. beneficial influence of ions during solar (SODIS) and photo-Fenton disinfection of *E. coli* in water: (Bi)carbonate, chloride, nitrate and nitrite effects. *Appl. Catal. B: Environ*. 270, 118877.

Ji, Y., Fan, Y., Liu, K., Kong, D., Lu, J., 2015. Thermo activated persulfate oxidation of antibiotic sulfamethoxazole and structurally related compounds. *Water Res*. 87, 1-9.

Wojnarovits, L., Toth, T., Takacs, E., 2020. Rate constants of carbonate radical anion reactions with molecules of environmental interest in aqueous solution: A review. *Sci. Total. Environ*. 717, 137219.

Golshan, M., Kakavandi, B., Ahmadi, M., Azizi, M., 2018. Photocatalytic activation of peroxymonosulfate by TiO_2 anchored on cupper ferrite (TiO_2@$CuFe_2O_4$) into 2, 4-D degradation: Process feasibility, mechanism and pathway. *J. Hazard. Mater*. 359, 325-337.

Moradi, M., Moussavi, G., Yaghmaeian, K., Yazdanbakhsh, A., Srivastava, V., Sillanpaa, M., 2020. Synthesis of novel Ag-doped S-MgO nanosphere as an efficient UVA/LED activated photocatalyst for non-radical oxidation of diclofenac: Catalyst preparation and characterization and photocatalytic mechanistic evaluation. *Appl. Catal B: Environ*. 260, 118128.

De la Mora, E., Carmichael, I., Garman, E. F., 2011. Effective scavenging at cryotemperatures: further increasing the dose tolerance of protein crystals. *J. Synchrotron Radiat*. 18 (3), 346-357.

Xu, M., Deng, J., Cai, A., Ma, X., Li, J., Li, Q., Li, X., 2020c. Comparison of UVC and UVC/persulfate processes for tetracycline removal in water. *Chem. Eng. J*., 384, 123320.

Sheng, B., Huang, Y., Wang, Z., Yang, F., Ai, L., Liu, J., 2018. On peroxymonosulfate-based treatment of saline wastewater: when phosphate and chloride co-exist. *RSC Adv*. 8 (25), 13865-13870.

Rastogi, A., Al-Abed, S. R., Dionysiou, D. D., 2009. Sulfate radical-based ferrous–peroxymonosulfate oxidative system for PCBs degradation in aqueous and sediment systems. *Appl. Catal. B: Environ*. 85, 171-179.

Abdel Messih, M. F., Ahmed, M. A., Soltan, A., Anis, S. S., 2019. Synthesis and characterization of novel Ag/ZnO nanoparticles for photocatalytic degradation of methylene blue under UV and solar irradiation. *J. Phys. Chem. Solid*. 135, 109086.

Alharbi, S. K., Kang, J., Nghiem, L. D., van de Merwe, J. P., Leusch, F. D. L., Price, W. E., 2017. Photolysis and UV/H_2O_2 of diclofenac, sulfamethoxazole, carbamazepine, and trimethoprim: identification of their major

degradation products by ESI–LC–MS and assessment of the toxicity of reaction mixtures. *Process Saf. Environ. Prot*. 112, 222-234.